Journal of Geography and Cartography 2024, 7(2), 6909.
https://doi.org/10.24294/jgc.v7i2.6909

Review

Spectroscopic techniques for detecting naturally occurring radioactive nuclides in geology and water: A comprehensive review and health implications

Mohamed H. Fathy[1,*], Farha Shaban[1], Thowayba M. Fawzy[1], Dat Viet Nguyen[2], Ahmed M. Eldosouky[1]

[1] Geology Department, Faculty of Science, Suez University, Suez 43221, Egypt
[2] University of Science, Vietnam National University, Hanoi 334, Vietnam
*** Corresponding author:** Mohamed H. Fathy, Mohamed.HeFaK@sci.suezuni.edu.eg

CITATION

Fathy MH, Shaban F, Fawzy TM, et al. Spectroscopic techniques for detecting naturally occurring radioactive nuclides in geology and water: A comprehensive review and health implications. Journal of Geography and Cartography. 2024; 7(2): 6909. https://doi.org/10.24294/jgc.v7i2.6909

ARTICLE INFO

Received: 5 June 2024
Accepted: 24 June 2024
Available online: 11 July 2024

Abstract: Naturally occurring radionuclides can be categorized into two main groups: primordial and cosmogenic, based on their origin. Primordial radionuclides stem from the Earth's crust, occurring either individually or as part of decay chains. Conversely, cosmogenic radionuclides originate from extraterrestrial sources such as space, the sun, and nuclear reactions involving cosmic radiation and the Earth's atmosphere. Gamma-ray spectrometry is a widely employed method in Earth sciences for detecting naturally occurring radioactive materials (NORM). Its applications vary from environmental radiation monitoring to mining exploration, with a predominant focus on quantifying the content of uranium (U), thorium (Th), and potassium (K) in rocks and soils. These elements also serve as tracers in non-radioactive processes linked to NORM paragenesis. Furthermore, the heat generated by radioactive decay within rocks plays a pivotal role in deciphering the Earth's thermal history and interpreting data concerning continental heat flux in geophysical investigations. This paper provides a concise overview of current analytical and measuring techniques, with an emphasis on state-of-the-art mass spectrometric procedures and decay measurements. Earth scientists constantly seek information on the chemical composition of rocks, sediments, minerals, and fluids to comprehend the vast array of geological and geochemical processes. The historical precedence of geochemists in pioneering novel analytical techniques, often preceding their commercial availability, underscores the significance of such advancements. Geochemical analysis has long relied on atomic spectrometric techniques, such as X-ray fluorescence spectrometry (XRFS), renowned for its precision in analyzing solid materials, particularly major and trace elements in geological samples. XRFS proves invaluable in determining the major constituents of silicate and other rock types. This review elucidates the historical development and methodology of these techniques while showcasing their common applications in various geoscience research endeavors. Ultimately, this review aims to furnish readers with a comprehensive understanding of the fundamental concepts and potential applications of XRF, HPGes, and related technologies in geosciences. Lastly, future research directions and challenges confronting these technologies are briefly discussed.

Keywords: radioactivity; radionuclides; HPGe detector; NaI(Tl) detector; LSC detector

1. Introduction

Cosmic beams and naturally radioactive components make up the natural radiation environment. A parcel of the materials is primordial, cosmogenic, and naturally occurring due to the radioactive change of compounds delivered by these forms. Their physical characteristics and changes over time are related to their radiological significance [1]. The primordial radionuclides are inferred from the

outside of the crust and may exist alone or as a portion of a decay chain. Illustrations of decay series components that are as often as possible found in gamma-spectroscopic perceptions are the uranium series' 224Ac and 214Bi; of the radionuclides that occur independently, 40K is the most common in natural estimations. On the other hand, the source of cosmogenic radionuclides is found in space, the sun, and atomic reactions, including cosmic radiation and the earth's atmosphere. Through air blending or precipitation, radionuclides are brought down to the Earth's surface. These radionuclides incorporate 7Be and 14C as illustrations [2].

Due to their possibly disastrous impacts on wellbeing, naturally occurring primordial radionuclides and the ionizing radiations they go with in encompassing natural compartments are of incredible concern [3–8]. Radiation introduction can lead to a number of health issues, including lung cancer, bone variations from the NORM (naturally occurring radioactive material), renal failure, and kidney breakdown. Primordial radionuclide dispersion in different natural fragments (such as sediment, soil, sand, dust, and water) is frequently impacted by local geomorphological, geological, climatic, and geochemical highlights as well as weathering process(es) [9]. Norms in soil or sediment are regularly connected to exposure to outside radiation, be that as it may, vaporous 222Rn inward breath ought to not be ignored. The primary source of natural radiation is radon, a naturally occurring gas that comes from rock and soil. People breathe in and consume radioactive materials on a daily basis from food, water, and the air. Radiation exposure can come from both external and internal sources. When a radionuclide is breathed, swallowed, or enters the bloodstream in any other way (by injection, for example, or through wounds), internal exposure to ionizing radiation takes place. Internal exposure ends when the radionuclide leaves the body on its own (via excreta, for example) or as a consequence of a therapeutic intervention [10].

Water exposure to radionuclides can happen in a variety of ways, but since surrounding water sources contain low amounts of primordial Norms, the impacts appear to be irrelevant [11]. Not at all like water, radionuclides are shown in street dust and cannot be ignored. Street dust exposures to ionizing radiation from Norms are not constrained to outside pathways (that disregard 222Rn absorption), such as soil or sediment. Breathing in street dust and its related Norms can enter the respiratory system [12]. Ordinarily related to better dust frameworks (diameter < 2 μm), Norms have the capacity to move over longer distances and pose posture wellbeing dangers to individuals due to their ability to enter the respiratory system [3,4]. There has been a critical resurgence in thinking about natural radioactivity in recent years. One clarification for this is the common rise in significance and request of nuclear science, of which this field is a portion.

The consideration of the characteristics and events of thorium, the parent of most known natural radionuclides, has been provoked by its practical significance as a source of raw materials for nuclear energy. Furthermore, it has been found that natural radioactivity is a phenomenon with far greater changeability and hereditary incidence than previously thought. Numerous earth researchers have utilized nuclear technologies in their investigations since the well-established and, as of late, found geological results of radioactivity's presence in the natural world. Radionuclides that naturally emerge and have lives extending from billions of a long time to less than a

diminutive can give experiences into a wide range of occasions, from cosmic history to micrometeorology. In any case, nature has appeared to be a valuable research facility accomplice for nuclear researchers, having the capacity to quicken particles to energies well past their claim capabilities and having the foreknowledge to start tests for them millions of years ago [13].

There are changing degrees of radioactivity in all rocks and soils. The 40K, 232Th, and 238U naturally occurring radioisotopes are the most predominant on Earth's surface. It is apparent from watching different inquiries about radioisotope concentrations in diverse sorts of rocks that this is same sort of rock [14–17] ordinarily shows a wide range of concentration values. However, certain patterns can be observed. For instance, felsic igneous rocks ordinarily have higher levels than sedimentary rocks. The rate at which people absorb outside gamma doses from the environment is impacted by the radioactivity of rocks. As a result, it's critical to gauge the radioactivity of rocks and comprehend how radioisotope dynamics influence the environment, human health, and development techniques.

The present review is concerned mainly with material published with references to a few prior works that are relevant to later advancements. The number of publications in this range is expanding quickly each year. In this research, we will center on the modern applications of radioactivity and spectrometry and highlight the case studies, their methods, and how they were done. These applications will be in distinctive areas, but the primary center will be in the geology field. In the next sections, we will show the applications in conversation, starting with their methodology.

2. Methodology

Nuclear radiation detectors became fundamental gadgets when radioactive sources were utilized in different spaces like health physics, industry, energy, and environmental applications. This is since radiation poses a health hazard [18]. The gadget that changes radiation energy into an electrical signal is called a detector. It is the radiation escalated that is created at the instrument's output after being digitally processed. In spite of the fact that these detectors work on different speculations, they eventually show the radiation output. a variety of radiation detectors for X-rays, UV, visible, and infrared light [19]. In this section, we will discuss a few of the most commonly utilized methods and detectors, and how they work, and their principles.

2.1. High purity germanium detector

A non-destructive method for evaluating the radioactive concentration of man-made and natural radionuclides in the environment is gamma-ray spectrometry utilizing germanium detectors. The earlier information on the full-energy peak efficiency at each photon energy for a certain measuring geometry is vital in order to determine the activity for each radionuclide. Hence, in order to continue, an efficiency calibration must be performed previously, utilizing a standard radioactive source that has the same shape, density, and chemical composition as the sample being examined. Nevertheless, these necessities are regularly not taken care of. It too proposes the issue that each sample configuration requires an efficiency calibration [20].

The number of photons discharged from the source and absorbed by the detector is the most pivotal step in estimations performed with a gamma-ray spectrometer. The capacity of a detector to absolutely and reliably detect and measure gamma radiation discharged by a radioactive source is known as detector efficiency. Different efficiency sorts, including intrinsic, photopeak, relative, and absolute efficiencies, are fundamental to precisely detecting and measuring gamma-ray radiation transmitted from radioactive sources [21].

Early in the 1980s, high purity germanium (HPGe) detectors were made available. They are planned to detect excited nucleus energies with more penetration power than can be measured with conventional junction and surface barrier detectors [22]. Liquid nitrogen is utilized to chill them in order to stop breakdowns and minimize electrical spillage. When compared to other sorts of radiation detectors, high purity germanium (HPGe) detectors can clearly perceive close-by energy peaks and give sufficient data to reliably and precisely recognize radionuclides from their gamma-ray radiation [23].

Semiconductors, or bunch four elements in the periodic table, are utilized to make the HPGe detectors. Three band gaps are shown in semiconductor materials: the valence band, the forbidden band, and the conduction band. The conduction band is empty, and the valence band is filled at the absolute temperature. Energized electrons go from the valence band into the conduction band, where they shape an empty zone known as a “hole”. When an electric field is present, current is delivered by the movement of the electrons and holes in the valence and conduction bands. There are the same number of holes and electrons in a pure semiconductor. A semiconductor’s band gap sets up the greatest number of energy carriers per signal. Germanium has a band gap energy of generally 0.6 eV, compared to 1.1 eV for silicon [24].

Through the deliberate presentation of impurities from group three or bunch five elements, a process known as “doping,” the conducting properties of these materials can be conveniently altered. The material is an N-type semiconductor if the impurities are group V elements since more electrons are given to the system. In any case, the material is alluded to as a P-type semiconductor if the impurities are from group three elements since fewer electrons are contributed to the system [25]. The P-N junction in the material was made by the two sorts of semiconductors. At this minute, the electrons and holes will clear past one another to deliver an electrical pulse. When an ionizing adiation ionizes a semiconductor material, the charges are straightforwardly collected by the high purity germanium (HPGe) detectors. Charge carriers, or electron-hole pairs, are made when a photon is interatomic with its substance. There will be an electron hole pair created inside the depletion layer as a result of an external particle entering the depletion layer (between the P-N junction). When an external particle enters the depletion layer, it essentially collides with the atoms and molecules in that region and transfers energy. The electrons in the valance band of that specific depletion layer will then absorb that energy and jump to the conduction band when that happens. These carriers are at that point cleared over one another and collected at the electrodes. The charge is closely related to the incident gamma photon’s energy [23].

In modern gamma-ray spectroscopy, HPGe detectors have widespread application owing to their outstanding output efficiency and fine energy resolution. The distance between the source and detector, calibrator dimensions, shielding

thickness, and incoming gamma ray energy all impact the HPGe detector's absolute efficiency, as recent studies have shown [26].

2.1.1. Parts of HPGe

Germanium is not liked by many detectors due to the need to cool them to liquid nitrogen temperatures. This is caused by the fact that the element has a relatively narrow band gap, which requires cooling so as to reduce the thermal generation of charge carriers to an acceptable level. Inadequate cooling of these devices causes noise from leakage currents that affects detector energy resolution. It should be noted that germanium's bandgap is extremely small (Egap = 0.67 eV). When it is cooled down to −195.8 ℃ (the temperature of liquid nitrogen), the excitations of valence electrons decrease, thereby allowing only gamma-rays interactions to provide an electron with enough energy to cross this gap into the conduction band. For this reason, most HPGe detectors are fitted with cryostats, while their crystals are enclosed in an evacuated metal holder known as the detector.

To avoid low-energy photon attenuation, the detector holder and endcap are made thin. The holder is ordinarily constructed from aluminum with a thickness of about 1 mm. The end cap is equally made of aluminum, analogously. The HPGe crystal is in the holder, and it is in direct thermal contact with a cold finger, which is a metallic rod. The transfer of heat from the assembly to the nitrogen container is facilitated by this cold finger. In general, the cryostat is made up of a vacuum metal canister, cold fingers, and a Dewar flask for the liquid nitrogen cryogenics system.

The germanium detector preamplifier is typically part of the cryostat itself. In order to minimize the total capacitance, the preamplifier is placed in close proximity to both detectors and is also cold-shielded. The cryostat has a vacuum enclosure that ends at the Dewar, containing liquid nitrogen, into which the cold finger extends. The Ge cryostat must be kept at a very low temperature, so it is immersed in liquid nitrogen. The liquid nitrogen remains at −195.8 ℃ because its gradual boiling releases nitrogen gas, thereby keeping the system insulated from thermal energy. Depending on their size and configuration, vacuum flasks can retain their contents for hours or weeks.

One major inconvenience of using liquid nitrogen for cooling is the time it takes the detector reach operational temperature. Another is that we can't let it warm up when in use. However, unlike HPGe detectors, which need to be kept at room temperature all the time they are not being used, Ge(Li) crystals should never be allowed to warm up, as this would cause lithium within them to drift out and damage the crystal, thus permanently break the detector.

There are advanced commercial systems nowadays that can use various modern cooling methods, like a pulse tube cooler and others, besides liquid nitrogen cooling. This new cooling system only requires electricity to work, and no LN2 is needed (**Figure 1**), making it a better option as it is more convenient and efficient.

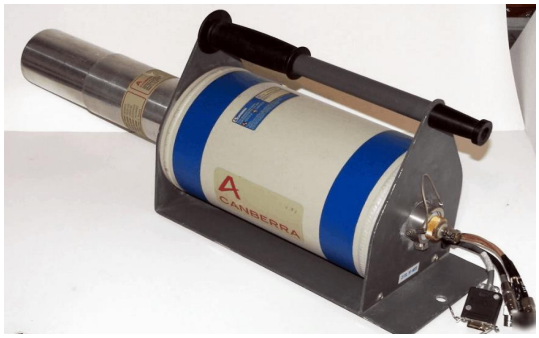

Figure 1. HPGe detector with LN2 cryostat [27].

2.1.2. Principle of operation

When ionizing radiation enters the germanium crystal of the detector, it interacts with the semiconductor material. A powerful photon passing through the detector triggers the ionization of atoms in the semiconductor, leading to the generation of pairs of electrons and holes. The number of electron-hole pairs produced is linked to the energy of the radiation interacting with the semiconductor. As a result, many electrons move from the valence band to the conduction band, creating a number of holes in the valence band.

Germanium, because of its property to maintain a sensitive layer measuring in centimeters, can fully capture high-energy photons (up to a few MeV). When subjected to a field, both electrons and holes move toward the electrodes, resulting in the creation of a signal, in an external circuit. The pulse of this signal contains details, about the power of the radiation exposure. Additionally, the rate at which these signals occur over a period of time gives us clues about the strength of the radiation.

In all cases, a photon emits part of its energy along the path and may be completely absorbed. When a 1 MeV photon is completely absorbed, it gives rise to about 3×10^5 electron-hole pairs. Compared with the total number of free carriers in an intrinsic semiconductor of 1 cm^3, this figure is rather small.

Thermal excitation, which is dominant in germanium-based detectors operating at room temperature, is not the only factor that causes ionization of the semiconductor atoms when particles pass through the detector. Dopants, impurities, and lattice irregularities are responsible for this phenomenon, and it depends largely on the *E*gap (energy gap) of the material, which for germanium is quite small (*E*gap = 0.67 eV) (**Figure 2**). Therefore, thermal excitation produces noise in detectors, and thus active cooling has to be applied to some kinds of semiconductors, such as germanium.

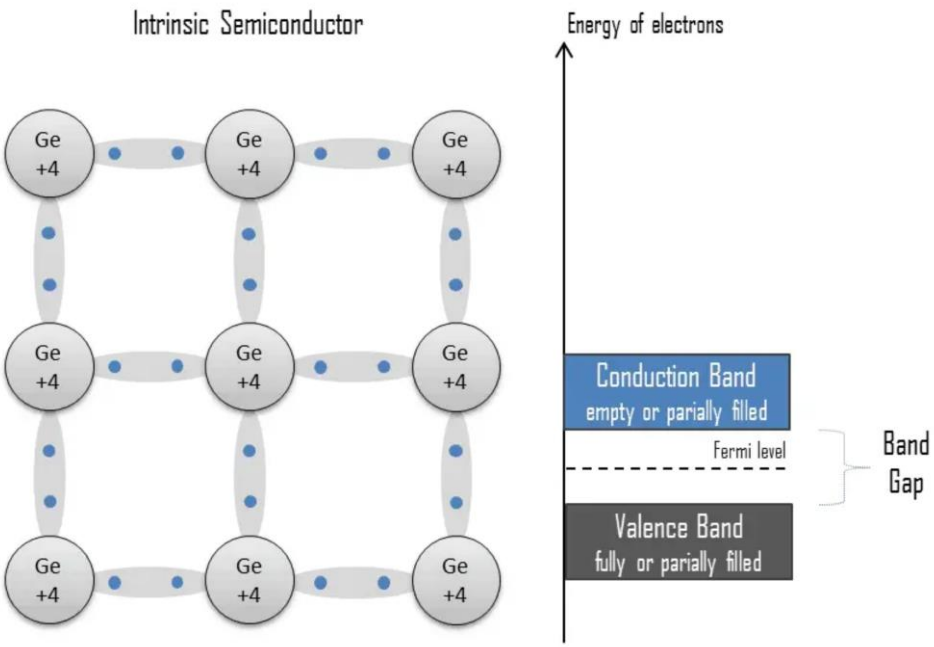

Figure 2. The influence of Egap on thermal excitation [27].

It deserves keeping in mind that a 1 cm^3 example of pure germanium at 20 ℃ consists of about 42 × 10^{22} atoms in addition to approximately 2.5 × 10^{13} complimentary electrons together with 2.5 × 10^{13} openings that are constantly produced from thermal power. Subsequently, the signal-to-noise proportion (S/N) is influenced [27].

2.1.3. Efficiency calibration

Using HPGe detectors, an efficiency calibration technique has been devised to assess the radioactivity of volume samples. The samples must be measured using the same measuring parameters as those used to calibrate the device in order to get accurate results [28].

A set of photopeak efficiencies over the energy region of interest, or a detection efficiency curve, must be known ahead of time in order to use the method. In addition to the detection technology, the sample shape and sample matrix with varying ambient sample densities and heights affect the detection efficiency curve. Since mass attenuation coefficients (μm) in environmental samples vary only little between samples, sample chemical composition variability is not a significant issue. Monte-Carlo calculations [29,30] can be used to estimate this effect or modeling [31]. Matrices increased [32]. In this instance, it is possible to experimentally determine and fit an efficiency curve for a wide range of matrices and energies. In order to achieve this goal, the standards' composition should as nearly resemble the samples' density, attenuation factors, and activity concentrations as feasible [33,34].

In order to reduce the deviation in the measured activity, the calibration standard source needs to have physical dimensions, a chemical composition, and a density similar to the samples that will be tested. In terms of geometry, if the container has the same dimensions and all of the samples and the standard source's heights are similar, the variance can be nearly eliminated.

2.1.4. Quality control

"In-house procedures" might be used to prepare the standards. This can be achieved by uniformly adding certified and traceable radionuclide solutions into inactive matrices that have the same density and composition as the material that needs to be tested. Like any other analysis method, γ-ray spectrometry requires standard samples to obtain the most precise experimental efficiency calibration in order to perform a quantitative analysis. However, if many configurations (e.g., different γ-ray detectors, geometries, densities, and sample shapes) are present, it can be time-consuming [35].

In order to calculate the activity of the various radionuclides contained in a sample, radioactive sources were prepared from two different standards, such as mixed standard QCY40, which contained 210Pb, 241Am, 109Cd, and 57Co, and standard QCY48, which contained 241Am, 109Cd, 57Co, 139Ce, 113Sn, 85Sr, 137Cs, 88Y, and 60Co. In terms of the measurement setups, we are pouring a certain volume of radioactive solution into a bottle that is partially filled with soil in order to prepare aqueous sources. The bottle is then consistently filled to the same height. Once the homogeneous soil has been added to the bottle until it reaches the required volume (weight or height), the bottles were sealed hermetically with a screw cap at the end.

2.1.5. Energy measurement

We measure the soil by itself in the same vial since it contains some naturally occurring radioactivity. By comparing the activity of the bottles with standard solution sources, the natural radioactivity of the soil was calibrated. At ZSR, gamma-ray data is analyzed using the GW program. The net count rate in the full-energy peak is then divided by the decay corrected gamma-ray emission rate of the standard source to determine the absolute detector efficiency at that energy [36].

2.2. Thallium activated sodium iodide detector NaI(Tl)

The NaI(Tl) scintillation detectors are one of the most commonly used detector systems used to measure gamma-ray detection (**Figure 3**). This can be explained by their low cost compared to HPGe detectors, high stability against thermal events and weather conditions (namely because they do not need additional cooling devices), etc. Furthermore, our NaI(Tl) scintillation detectors show huge detection efficiency [37].

The NaI(Tl) detector provides valuable benefits to users by allowing a variety of gamma spectroscopy studies to be performed at room temperature. This feature proves to be very beneficial for researchers. Additionally, the use of NaI(Tl) detectors with large surface areas effectively reduces the time required for measurements [38–40]. Unlike HPGe detectors, NaI(Tl) detectors offer the advantage of high absorption efficiency due to the presence of thallium (Z = 81) in their structure. This results in a high photo peak/Compton ratio.

Then again, HPGe detectors are known for their higher resolution capabilities [41] In the detection of gamma rays utilizing a NaI(Tl) detector, the physical interactions between the gamma rays and the crystal of the detector are well caught on, counting the photoelectric effect, Compton scattering, and pair production. To successfully measure gamma rays with a NaI(Tl) detector, it is fundamental to get parameters such as reaction work, energy resolution, and their relationship with

experimental setup conditions like geometry, gamma ray energies, and source distance from the detector. Whereas experimental methods can give a few of this data, they are constrained by experimental conditions.

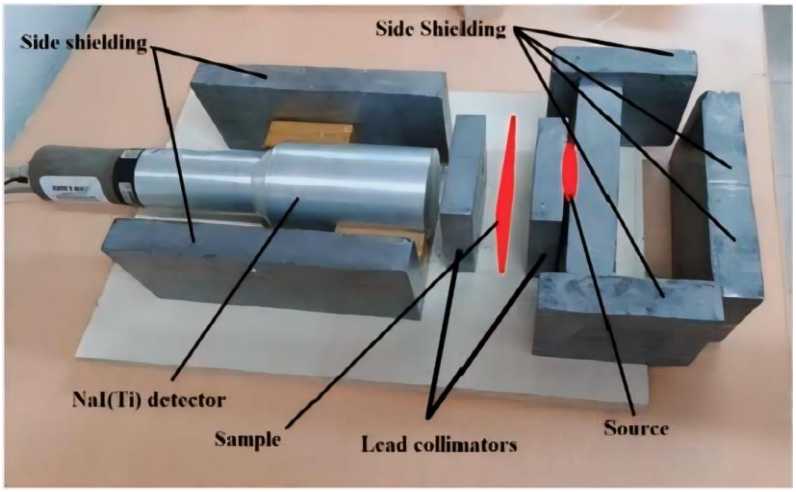

Figure 3. NaI(Tl) detector and its components [48].

Instead, Monte Carlo simulations, including the FLUKA simulation tool, provide the capability to gain a huge range of parameters without energy or setup obstacles. FLUKA is a flexible tool for calculating particle transport and interactions with matter, with programs ranging from accelerator shielding to detector design, dosimetry, and more.

FLUKA sticks out from other Monte Carlo applications because of its dual capability to function in both biased and absolutely analog modes, allowing for the prediction of fluctuations, signal coincidences, and uncommon events at the same time as presenting a variety of statistical techniques to investigate attenuations over many orders of magnitude [42,43].

Many publications have used FLUKA and many other Monte Carlo codes for research purposes. Among these publications, a notable part focuses on modeling the 3"×3" NaI(Tl) scintillation detector [44–48] some of which relate to the measurements performed for this specific target [47] and some of them are linked to the use of radiation doses [48].

The energy resolution of the 3" × 3" NaI(Tl) detector at about 49 keV turned out to be 7.4% for 662 keV gamma rays. This is close to the typical energy resolution reported for a NaI(Tl) detector detecting 662 keV gamma rays emitted from a 137Cs source. The resolution values of cylindrical detectors of this type are typically between 7.0% and 8.5%, and these values can be easily achieved with commercially available detectors [48].

The performance ranges from 186.1 to 2614 keV, showing two distinct regions, indicating variation in detector performance behavior due to attenuation and absorption processes. At lower photon energies, the absolute efficiency of the detector continues to increase as the attenuation of the radioactive source is significantly reduced. The observed gamma energy peak depends on detector and source characteristics. Beyond a few hundred keV, the performance gradually decreases. In the case of the NaI(Tl) detector, the absolute detection efficiency cannot be expressed

as a single value. Detection efficiency is highly dependent on factors such as gamma-ray energy, source location, activity, and the shape and composition of the source detector system, all of which are contextual variables [49].

Most of the time, standard spectra obtained using at least three concrete pads enriched in K, U, and Th are used to calibrate portable gamma-ray spectrometers for use in natural radioactivity measurements. A background is represented by a pad free of radioactivity [50,51]. Typically, these pads have an area of at least 2 m^2 and a thickness of 0.5 m [52]. A more affordable and practically impractical approach was used in place of designing an ideal pad with a single radionuclide within and a flawlessly homogenous distribution of radioisotopes across its volume. The detector's performance is ascertained through two calibration stages. The process that allowed the obtained spectrum to be understood as a function of the energy connected to the decay events is known as energy calibration. This depends on how much radioactive element content there is in the system being studied. Finding the parameters that connected the count rate under a photopeak to the radionuclide's soil radioactivity concentration (BqKg-1) and air dose rate was the second step in the calibration process.

2.2.1. Energy calibration

Weighing reference materials from the International Atomic Energy Agency (IAEA) such as RGU, RGK, and RGTh in petri dishes allowed for the energy calibration of the detector. To illustrate the non-uniform dispersion of the radionuclide in the surroundings, standard materials were placed in petri dishes. The detector, which stood 140 mm tall, was positioned directly above the setup. This was permitted because the goal was to collect only the naturally occurring radioactivity that resulted from the low-gamma-emitting radionuclides found in the soil. The spectrum analysis technique used was the Window Analysis Method (WAM). This technique just takes the spectrum's region of interest into account [50]. Therefore, the single peak released by 40K at 1460 keV was studied to determine the concentration of potassium. Uranium, 238U, was found at 1765 keV from 214Bi, while Thorium, 232Th, was found by 208Tl's gamma rays at 2614 keV. Following a predetermined 300 s [53], the channels of the various photopeaks that corresponded to the gamma energies were recognized when a spectrum was captured. The software's calibration option was chosen, and each peak of interest's gamma energies were inserted against its channel number to complete the calibration process. The software consequently created a relationship between the gamma energy and the channel number. To acquire count rates owing to each radionuclide under its reference peak, the regions of interest (ROI) were carefully established around these photo peaks. Using the conversion parameters, these count rates were translated to radionuclide soil activity concentration.

2.2.2. Efficiency calibration

We can only infer the distribution of energy depositions in the detector's active volume from the pulse height distribution that was previously acquired from the detector and MCA. Efficiency calibration connecting the number of recorded counts in the detector to the ground deposition activity level is necessary for a radionuclide-specific measurement of the activity [54]. According to Beck et al. [55], the soil radioactivity concentration of the radionuclide causing the peak is correlated with the

number of counts per second, acquired under a photopeak due to a specific gamma energy.

2.3. Liquid scintillation counting (LSC) technique

Ernest Rutherford used luminescence to detect α particles, making it one of the first techniques to measure radioactivity. Initially, the human eye could detect pulses of light. However, the advent of sensitive photodetectors, such as photomultiplier tubes (PMTs), paved the way for the development of scintillation counters. In 1950 [56,57], two independent groups reported that organic solutions could be used to detect β particles, leading to the advent of liquid scintillation. The first commercial clock was produced by Packard Instruments in 1953, and since then, many complex data processing techniques have been incorporated into LSC clocks following the invention of the microprocessor. Commercial production of LSC counters peaked around 1975, but there was then a steady decline due to the emergence of alternative non-radioactive monitoring techniques for biological purposes. At the same time, there was growing interest in LSC techniques in the field of radionuclide measurement, especially after the publication in 1979 of two quantitative LSC measurement methods: the triple coincidence ratio (TDCR) [58] and the CIEMAT/NIST method in 1982 [59]. Currently, the main focus of the commercial LSC market lies on providing low activity measurements and developing liquid scintillators with reduced toxicity levels.

2.3.1. Liquid scintillators composition

A liquid scintillator is capable of changing a portion of the energy from ionizing radiation into light. It is basically composed of scintillator molecules that are dissolved in an organic solvent. In order to tailor the liquid scintillation cocktail for particular applications, extra components such as a secondary solvent, secondary scintillator, surfactant, extractant, and quencher are added (**Figure 4**). The composition of the liquid scintillation cocktail ought to facilitate efficient transfer of energy between the solvent and scintillator solute while also allowing for the coexistence of the aqueous radioactive solution with the organic solvent. Be that as it may, these requirements can now and then clash, making the improvement of an ideal liquid scintillator cocktail a matter of compromise.

The solvent plays a vital role in the cocktail as it absorbs the energy radiated by charged particles from the radionuclide and transfers this energy to the fluorescent molecules. Aromatic organic molecules are commonly utilized as liquid scintillator solvents. Whereas benzene and toluene were already utilized, less poisonous solvents like xylene or pseudocumene are presently favored. In recent years, a new generation of aromatic solvents, such as di-isopropyl naphthalene (Din), phenyl xylyl ethane (PXE), and dodecylbenzene (DB), have been developed. These solvents offer reduced toxicity and higher flash points, although they may show lower stability and production consistency. It is vital to note that these new solvents are mixtures of different products and isomers, and the producer cannot ensure that the composition of products sold under the same commercial title will stay unaltered. Solvents have lower toxicity and higher flash points but may have lower stability and consistent production. The new solvents are mixtures of various products and isomers, so the producer cannot guarantee the composition remains unchanged for products sold

under the same name.

The primary scintillator, displayed in concentrations extending from 5 g/L to 10 g/L of solvent, is responsible for converting the excitation energy of the solvent molecules into light. Commonly utilized primary scintillators include 1,5-diphenyloxazole (PPO), p-terphenyl (TP), 2-phenyl-5-(4-diphenyl)-1,3,4-oxadiazole (PBD), and (2-(4-t-butylphenyl)-5-(4-biphenyl)-1,3,4-oxadiazole (butyl-PBD). However, other fluorescent molecules, such as laser dyes, can also be utilized in this part.

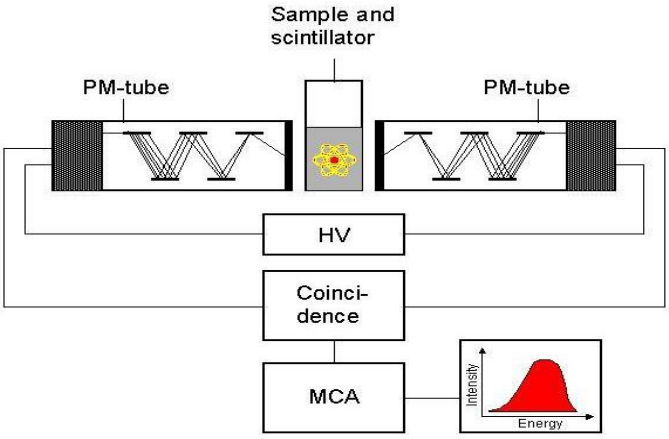

Figure 1. LCS detector and its components [60].

The secondary scintillator is utilized in LS cocktails to adjust the scintillator emission range to match the greatest sensitivity of the photocathodes of PMT. It is ordinarily shown in a mass concentration of roughly 0.5 g/L of solvent. The scintillators utilized for this reason include 1,4-di-(2-(5-phenyloxazolyl)) benzene (POPOP), p-bis-(o-methyl styryl) benzene (bis-MSB), or 1,4-di-(2-(4-methyl-5-phenyloxazolyl)) benzene (DM-POPOP).

In LS cocktails that are water-miscible, the addition of a surfactant is necessary to guarantee the miscibility of the radioactive aqueous sample with the primary solvent-solute system. The surfactants are ordinarily shown in amounts up to 30% by weight. To upgrade detection efficiency, non-ionic aromatic surfactants with great energy propagation properties are favored. One such surfactant is iso-octyl phenoxy-poly ethoxy ethanol (Triton X-100®). On the other hand, a polar molecule that allows the coexistence of organic and aqueous phases inside a constrained volume range can be utilized as a substitution for surfactants. Whereas ethanol was previously utilized for this reason, phenoxyethanol is presently favored due to its energy transfer properties, which help limit the reduction of scintillator light yield caused by the addition of the surfactant.

Certain LS cocktails contain extractant molecules in molar concentrations of roughly 10^{-2} mol/L. These extractants facilitate the liquid-liquid extraction of the radionuclide from the aqueous phase into the scintillator organic phase. Organic extractants such as di-2-ethylhexylphosphoric acid (HDEHP) or tri-n-octyl phosphine (TOPO) are commonly utilized. These extractants not only enhance the stability of the scintillator but also improve the detection efficiency for particular elements.

In some LS cocktails, a secondary solvent is presented in mass concentrations of

up to 200 g/L to improve the differentiation between electron and alpha particle responses. Aromatic molecules with long half-life triplet states, such as naphthalene or naphthalene compounds, are regularly utilized for this purpose.

If wanted, a chemical quencher can be added to LSC cocktails to decrease the scintillation efficiency.

2.3.2. Transfer of energy in the scintillator

Radionuclide decay radiation traverses the liquid scintillator and primarily interacts with the solvent molecules. The interaction between radiation and matter generates incident electrons or secondary electrons, which in turn excite or ionize the solvent molecules. In any case, a critical portion of the incident energy is dissipated as heat.

Approximately 10% of the energy is transferred to excited singlet and triplet molecular states. Singlets rapidly return to their ground state S1 through de-excitation, whereas triplets lose their energy through internal change and cannot directly transmit light. All things considered, bimolecular triplet-triplet reactions can deliver singlet states, enabling light emission. The extents of excitation and ionization depend on the stopping power and energy of the incident particle, with alpha particles causing more ionizations compared to electrons. Both ionization and excitation can result in fluorescence, but triplet production is more prominent in ionization.

The energy migrates from one solvent molecule to another within a sub-nanosecond timeframe until it is either trapped by a solute molecule or scattered as heat. These energy transfer processes happen without radiation. Fluorescence occurs when excited singlet states of the solute experience radiative de-excitation. The decay time constants for fluorescence are typically a few nanoseconds.

On the other hand, light production through de-excitation of triplet states, known as phosphorescence, is less likely as it requires triplet-triplet bimolecular reactions. Consequently, the decay time for phosphorescent emission is longer.

The spectrum of emitted photons is particular to the fluorescent solute and solvent species. If a secondary solute is shown, the energy transfer to it happens through radiation [61].

2.3.3. The CIEMAT/NIST method

The CIEMAT/NIST method is exemplified in **Figure 5**, where the initial step involves calculating the efficiency of a system with two PMTs in coincidence according to Peng and Li [62] with $P(E, \lambda)$ and $R = 2$. This calculation must be carried out for both the nuclide under investigation and a tracer nuclide, typically 3H. By introducing the free parameter $M = \lambda$, a connection between the counting efficiencies of the two radionuclides is established, allowing for the determination of the counting efficiency of the nuclide under study, $\varepsilon_{\text{nuclide}}$, in relation to the counting efficiency of the tracer, $\varepsilon_{\text{tracer}}$. This relationship is known as the 'efficiency curve'. Subsequently, the calibration curve, which represents the counting efficiency of the tracer, $\varepsilon_{\text{tracer}}$, as a function of the quenching indicator, QIP, is determined. This process involves preparing a series of approximately ten vials, each containing a scintillation cocktail and a known quantity of a tritium activity standard solution. Starting from the second sample, increasing amounts of a quenching agent are added to reduce the counting efficiency. Since the activities of the tritium samples are already known, the measured

net counting rates provide the counting efficiencies ε_{tracer}. Furthermore, the quenching indicator QIP is automatically measured for each sample using an external standard source integrated into the counter system.

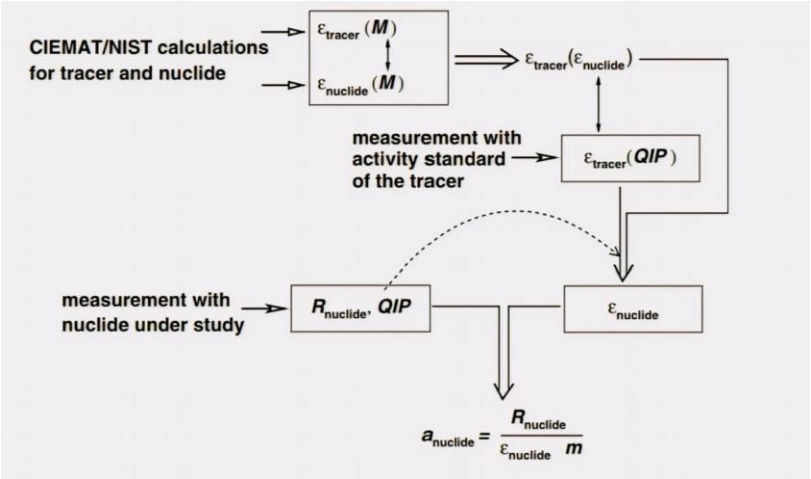

Figure 5. Illustration of the CIEMAT/NIST method [61].

R denotes the measured counting rate, *M* is the free parameter, QIP is the quench Indicating parameter, ε is the counting efficiency, $a_{nuclide}$ is the solution activity concentration and *m* is the mass of solution in an LSC sample.

In conclusion, a sample series is meticulously prepared using a solution of the nuclide being investigated. It is imperative that the sample composition and measuring geometry closely resemble those used in the calibration measurements. The counting rate and the quenching indicator QIP of the sample series are then accurately measured.

The QIP indicator enables the determination of the tracer efficiency from the calibration curve. Once the tracer efficiency is known, the nuclide efficiency can be determined using the efficiency curve. Consequently, all necessary information is available for calculating the activities of the samples and the activity concentration of the solution.

2.3.4. Quality control

Periodic global checks of the LS counter are essential, especially after significant changes in the counter. While the IEC 1304 standard provides guidance for conducting these checks [61], it is important to note that the document contains outdated information. Therefore, it is recommended to adhere to the principles outlined in the standard rather than strictly following the outdated details. Various checks, such as repeatability, reproducibility, fidelity, and linearity, should be performed using reference LS sources. Typically, pure organic 3H or 14C labeled scintillators enclosed in flame-sealed ampoules are used as reference sources. Although IEC 1304 suggests replacing these reference sources every five years, practical experience indicates that they can remain stable for decades if stored at a moderate temperature (below 20 ℃) in a dark environment. The linearity of the counter's performance can be assessed by employing a series of reference LS sources that exhibit progressively higher levels of activity. This particular test enables the identification of the operational range within which the counting rate remains accurate, while also providing a means to rectify any

counting bias that may occur beyond this range.

2.2.5. Calculation of energy spectra

The determination of the counting efficiencies necessitates the calculation of the energy spectrum that is transferred to the liquid scintillator, denoted as $S\epsilon$. This energy spectrum is normalized.

$$\int_0^{E\max} S(E)\mathrm{d}E = 1$$

This range encompasses electrons that originate either from the decay of the initial isotope or from rearrangement processes occurring in the shell of the daughter atom. Furthermore, photons resulting from the decay process can transfer energy to electrons through Compton scattering and the photoelectric effect. If the energy of the photon exceeds 1.022 MeV, it can also generate an electron-positron pair.

3. Case studies

In this section, we will discuss case studies where they used the methodologies mentioned before and how they used them in their experimental work in their research.

3.1. Intercomparison NaI(Tl) and HPGe spectrometry to studies of natural radioactivity on geological samples

A case study by Hung et al. [63].

3.1.1. Experimental setup

The NaI(Tl) detector's scintillation crystal is a cylindrical shape measuring 7.62 cm × 7.62 cm and is made by Canberra, Inc., USA. This detector is connected to an Osprey™ tube, which serves as a modern, all-in-one multi-channel analyzer (MCA) tube base designed to facilitate scintillation spectrometry [64].

Table 1. Parameters of the HPGe detector [63].

Main parameters	Geometrical parameters	Value
Relative efficiency		35%
Energy resolution (FWHM) at 1332 KeV (Co60)		2 KeV
Peak-to-Compton ratio (Co60)		66:1
Geometrical parameters of the detector	Window thickness (mm)	1.5
	Crystal-window distance (mm)	5
	Crystal dead layer thickness (outer) (mm)	0.46
	Crystal dead layer thickness (inner) (μm)	0.3
	Crystal length (mm)	50.1
	Crystal diameter (mm)	62.2
	Crystal hole depth (mm)	23
	Crystal hole diameter (mm)	7.5
	Side cap thickness (mm)	1.5
	Side cap diameter (external) (mm)	76.2

This integrated module comprises a high-voltage power supply (HVPS), a

preamplifier, and a comprehensive digital MCA. It is operable through a single cable connecting the Osprey™ to the control and information acquisition systems. The HPGe detector, given by Canberra, Inc., USA, is developed with a p-type high-purity germanium material (**Table 1**).

The concentration of 238U was determined by analyzing the activities of 226Ra (186.2 keV), 214Pb (241.9 keV, 295.2 keV, and 351.9 keV), and 214Bi (609.3 keV, 1120.3 keV, 1764.5 keV, and 2204.2 keV). On the other hand, the concentration of 232Th was calculated based on the activities of 212Pb (238.6 keV), 208Tl (583.2 keV, and 2614.5 keV), and 228Ac (338.3 keV, and 911.1 keV). The activity of 40K was determined directly from the gamma line at 1460.8 keV. The analysis of gamma rays' spectra and information processing were carried out utilizing Geniee 2K software, which was also utilized for the show and processing of spectra from both detectors. The acquisition time for background, reference, and samples was set at 86,400 s each. Peak identification and resolution of overlapping peaks were performed utilizing Colegram software [65].

3.1.2. Reference sample

The NaI(Tl) detector's efficiency was experimentally calibrated using three reference samples from the International Atomic Energy Agency [66]: RGK-1, RGTh-1, and RGU-1. These samples have mass activities of 14,000 ± 400 Bq/kg, 3250 ± 90 Bq/kg, and 4940 ± 30 Bq/kg, respectively. Moreover, the RGU-1 source was utilized to establish the standard curve of efficiency for the HPGe detector. This calibration was conducted inside the energy range of 46.5 keV to 2204.2 keV, particularly focusing on 210Pb (46.5 keV), 234Th (63.3 keV), 226Ra, 214Pb, and 214Bi (in equilibrium with its parent 238U with a mass activity of 4940 ± 30Bq/kg) for the evaluation of 238U.

In our analysis, we encountered a sample that emits gamma transitions of 186.2 keV and 185.7 keV, compared to 226Ra and 235U, respectively. By examining the count rate in the 186 keV region, we can apply a correction factor of 0.5709 to precisely determine the value of 226Ra and get an extra result for 235U [67]. The ACORES software is utilized to fit the experimental efficiency curves to a log-log polynomial [68] (see **Figure 6**).

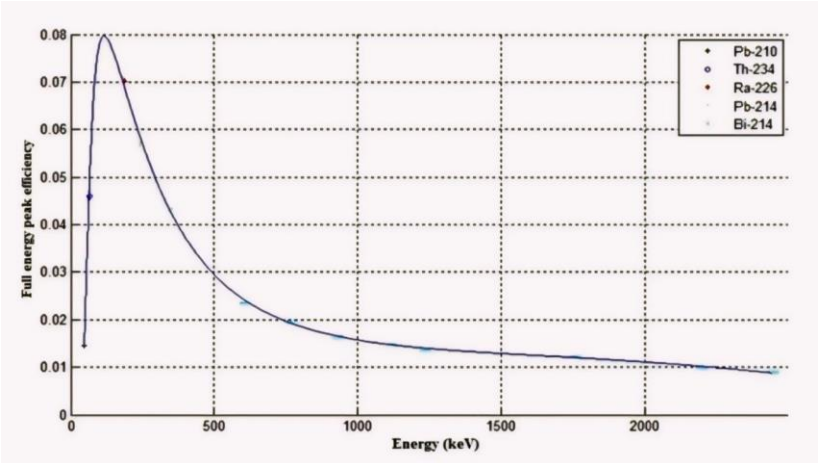

Figure 6. Experimental full energy peak efficiency calibration curve for volume source [63].

3.1.3. Sample data.

The Southern Geological Mapping Division collected the samples from a location in Vietnam's environment. Each area yielded more than 200 g of material, which was carefully collected and ground into dust. In this way, the samples underwent sieving and were set in cylindrical containers. These containers were, at that point, sealed off in the laboratory for a minimum of 30 days. This duration is significant to prevent any radon from escaping and to avoid any potential disequilibrium issues between 226Ra and its corresponding progenies (**Table 2**) [63].

Table 2. The information of the standard and the samples [64].

Sample	Mass (g)	Density (g/cm^3)
RGK-1	135	1.62
RGU-1	130	1.55
RGTh-1	119	1.42
S1	140	1.68
S2	116	1.39
S3	132	1.57
S4	136	1.63
S5	132	1.57

The cylindrical container, which housed both the standard and sample sources, had particular qualities. These included an external diameter of 75 mm, a wall thickness of 2 mm, and a bottom thickness of 2 mm. Besides, the container was filled to a height of 20 mm [63].

3.1.4. Results

The background and sample of both detectors **Figure 7a,b** were compared.

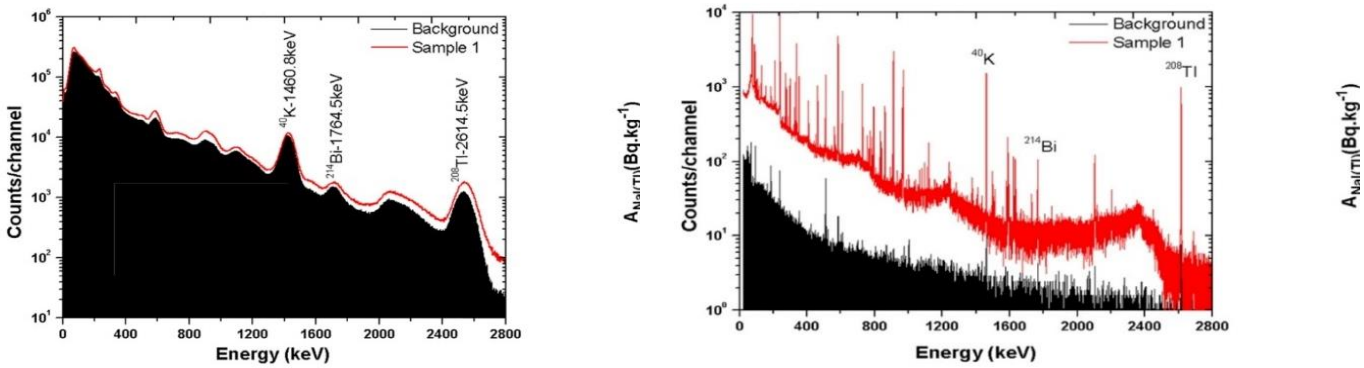

(a) **(b)**

Figure 7. Sample 1 and background spectra resulting from 86,400 s acquisition time; **(a)** for NaI(Tl); **(b)** for HPGe detectors respectively [63].

At first, the efficiency of the NaI(Tl) detector was experimentally calibrated using the kit standard to determine the activities of radionuclides in the sample. At the same time, the HPGe detector in the laboratory was utilized to measure the activities of the radionuclides in the sample. In accordance with Equation (1) [63], the mass activity

of radionuclide for each peak with energy *E* was calculated based on the net peak area, *Np€*, the relevant photon emission intensity, *I€*, the efficiency, *ε€* for the calibration conditions, acquisition live time (s), dry mass (kg), and the product of different correction coefficients such as coincidence summing, radioactive half-life.

$$A_i = \frac{NP(Ei)}{\varepsilon P(Ei) \times I(Ei) \times t \times m} \times IICi \quad (1)$$

The results, along with their corresponding combined standard uncertainties [69], are displayed in this study. The relative uncertainties mentioned in this paper are based on the combined standard uncertainties ($k = 1$). The computation of these uncertainties includes factors such as peak area, interpolation efficiency derived from a function, and the intensity of photon emission that is relevant to the analysis. To assess the performance of the estimation procedure for the samples, both detectors were utilized. The evaluation followed the approach utilized by the International Atomic Energy Agency (IAEA) in recent intercomparison exercises and proficiency tests [70].

The *U*-score is decided by utilizing the data obtained from the Nal(T) detector, the HPGe detector, and a standard deviation, as outlined in the subsequent formula:

$$U_{\text{score}} = \frac{A(\text{HPGe}) - A(\text{NaI(Tl)})}{0.1 \times A(\text{HPGe})}$$

The performance assessment of the Nal(TI) detector is considered satisfactory if the U_{score} is equal to or greater than 2. It is considered questionable if the *U*-score is greater than 2 but less than 3, and it is considered unsatisfactory if the *U*-score is equal to or greater than 3. The *A*(HpGe) represents the activity concentration value gotten from the HPGe detector, while the *A*(NaI(Tl)) represents the activity concentration result detailed by the NaI(TI) detector. The relative bias (RB) is calculated using the following equation:

$$RB = 100 \times \frac{|A(\text{HPGe}) - A(\text{NaI(Tl)})|}{A(\text{HPGe})}$$

Accuracy assessment: the findings are deemed satisfactory if:

$$\left|A(\text{HPGe}) - A\left(\text{NaI(Tl)}\right)\right| \leq 2.58 \times \sqrt{U_{\text{HPGe}}^2 + U_{\text{NaI(Tl)}}^2}$$

The standard uncertainties $U_{\text{NaI(Tl)}}$ and U_{HPGe}, along with a parameter of 2.58, are utilized to evaluate the probability of a result passing a test at a 99% confidence level.

The calculation of precision (*P*) assessment requires adherence to the prescribed formula:

$$P = 100\% \times \sqrt{\left(\frac{U_{\text{HPGe}}}{A_{\text{HPGe}}}\right)^2 + (\frac{U_{\text{NaI(Tl)}}}{A_{\text{NaI(Tl)}}})^2}$$

The NaI(Tl) detector results are regarded as satisfactory for precision when the specified condition is met:

$$P \leq \text{LAP}$$

In this investigation, we set the LAP (limit of acceptable precision) and MAB (maximum acceptable bias) at roughly 10% for each radionuclide. To accomplish the designation of "acceptable," the result must demonstrate satisfactory levels of accuracy and precision. If either precision or accuracy is regarded as "not acceptable," the RB is compared to the MAB. If RB < MAB, the result is labeled as a "warning"; on the other hand, if RB > MAB, the result is classified as "not acceptable." The

maximum deviation of the *U*-score is 0.52 for the radionuclides present in the samples, indicating that the values obtained from both the NaI(TI) and HPGe detectors meet the *U*-score criteria. Besides, there is a solid agreement in relative bias when utilizing both detectors.

The findings are illustrated in **Figure 8a–c**, which shows the relative activities of 238U, 232Th, and 40K, respectively. **Table 3** outlines the mass activities of the samples, with a maximum relative deviation of roughly 5% for both detectors, except for radionuclide 238U in sample (S2). Following the proficiency test protocol for assessing accuracy and precision, all radionuclides passed the evaluation. Consequently, the overall performance of the analytical determinations in the proficiency test meets the criteria for acceptability, with all results considered "acceptable" for the radionuclides present in the samples [63].

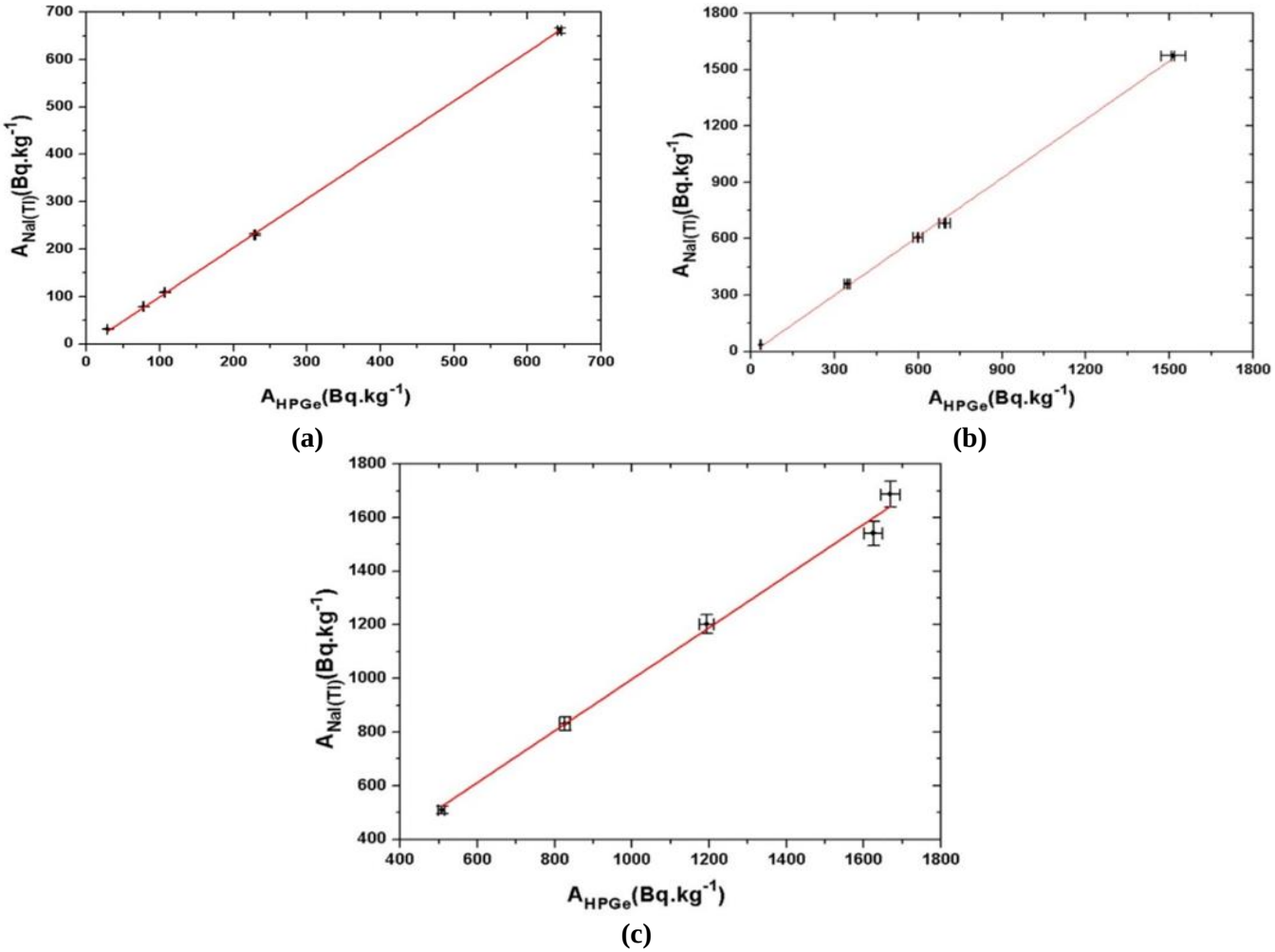

Figure 8. Relative function of radioactive of both detectors: **(a)** for 238U; **(b)** for 232Th; **(c)** for 40K respectively [63].

Table 3. Mass activities are measured using NaI(Tl) and HPGe detectors respectively [63].

	Mass activity (Bq·kg^{-1})					
	238U		**232Th**		**40K**	
Sample	**NaI(TI)**	**HPGe**	**NaI(TI)**	**HPGe**	**NaI(TI)**	**HPGe**
S1	78.65 ± 0.25	77.48 ± 0.52	681.84 ± 19.3	694.88 ± 2.49	1540.87 ± 44.54	1625.7 ± 23.8
S2	30.77 ± 0.77	28.58 ± 0.26	360.71 ± 10.38	345.3 ± 1.39	1202.4 ± 34.89	1193.54 ± 18.14
S3	230.28 ± 2.51	229.24 ± 1.21	606.43 ± 17.22	598.84 ± 2.21	1687.37 ± 48.74	1669.45 ± 24.45
S4	108.93 ± 0.53	106.83 ± 0.67	1573.62 ± 44.12	1513.33 ± 5.09	509.26 ± 15.06	507.37 ± 8.83
S5	661.29 ± 5.63	643.58 ± 3	35.32 ± 1.32	34.45 ± 0.28	831.3 ± 24.33	826.48 ± 13.45

3.2. Anomalous concentrations of radionuclides in the groundwater of Ede Area, southwestern Nigeria: A direct impact of geology

A case study by Adetunji et al. [71].

3.2.1. Methodology

In November (during the dry season), a study was conducted to sample groundwater in different zones of Ede. A total of 15 samples were collected utilizing a standardized sampling method. Out of these, ten samples were obtained from Ede town, whereas two samples each were collected from Iddo and Ekuro, and one sample from Iwoye communities. The sampling areas are denoted as S1–S15 on the geological map. Thirteen of the samples were taken from hand-dug wells, while the remaining two samples were extracted from boreholes. To guarantee the purity of the samples, plastic containers were used, which were first rinsed with distilled water to eliminate any foreign substances. Hence, the containers were further rinsed with the water sample collected from each particular area. To avoid any external contamination or mix-up with other water samples, the containers were firmly sealed and labeled accordingly.

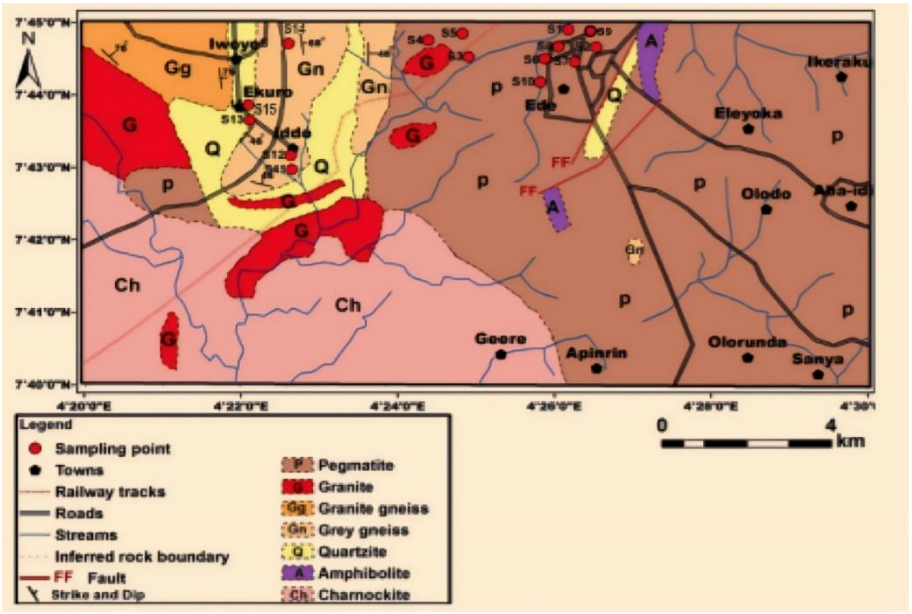

Figure 9. Geological map of Ede Area (the sampling points are indicated as S1–S15) [71].

The exact coordinates of sampling destinations were established utilizing a global positioning system (GPS) and, in this way, marked on the geological map of the research region (see **Figure 9**) [71].

The sodium iodide gamma spectrometer at the Centre for Energy Research and Development (CERD) at Obafemi Awolowo University, Ile-Ife, Nigeria, was utilized to determine the radionuclides present in the water. To prepare the water samples for analysis, hydrochloric acid was added. Each water sample, measuring 250 cm^3, was then carefully stored in an airtight and properly sealed container inside the laboratory for a duration of 28 days. This period permitted the establishment of secular equilibrium between isotopes and their respective daughters before conducting gamma-ray spectrometry analysis. It is worth noting that this specific technique has been broadly utilized by various analysts in the field [72–74].

After this time period, the hermetically sealed containers were individually positioned inside a strong lead enclosure and secured with a substantial seal. Attached to the lead enclosure was a sodium iodide radiation detector that produced electronic charges through ionization due to gamma-ray emissions. The spectrometer is comprised of a Canberra 7.6 cm by 7.6 cm NaI(TI) detector connected to a Canberra Series 10 Plus Multichannel Analyzer (MCA) through a preamplifier base. Protection of the environment from radiation was fulfilled by utilizing a Canberra 10-cm-thick lead castle [75].

Counting was conducted for a duration of 10 h due to the minimal natural activities of radionuclides present in the water. The spectrum was evaluated, and the calculation of the area underneath the photopeaks was carried out utilizing the MCA algorithm. The significant photo peaks detected in the samples' spectra were recognized as originating from radionuclides inside the natural decay series of 238U and 232Th, as well as the non-series 40K. To identify the gamma energy peaks, the spectra analysis software SAMPO 90 was utilized to compare them with a library of potential radionuclides [76–80].

3.2.2. Results

The data on radioactivity levels in the media samples are shown in **Table 4**. Radioactivity is measured in the Becquerel (Bq), with 1 Bq equivalent to 1 disintegration per second. The recommended levels for radioactivity in drinking water are expressed as the activity concentration of the radionuclide per liter, denoted as Bq/L. In the study area, the uranium-238 series (radon-222 and radium-228) were identified as the most predominant radionuclides in water. The activity concentration of the uranium series ranged from 7.24 ± 0.24 to 23.76 ± 0.31 Bq/L, with an average of 13.256 Bq/L over the four communities. Specifically, Ede had an average activity concentration of 13.645 Bq/L, ranging from 23.76 ± 0.31 to 7.24 ± 0.24 Bq/L. This shows that the average radioactivity level in Ede surpasses the regional average (13.256 Bq/L) for the whole area by roughly 0.389 Bq/L. Iddo and Ekuro had average values of 11.685 ± 0.3 Bq/L and 13.49 ± 0.7 Bq/L, respectively, while Iwoye recorded a value of 12.04 ± 0.23 Bq/L.

The concentration of thorium series activity in the whole area varies from 6.42 ± 0.53 to 20.97 ± 0.66 Bq/L, with an average value of 10.51 Bq/L. In contrast, samples collected from Ede display a range of values from 20.97 ± 0.66 Bq/L to 4.08 ± 0.89

Bq/L, with an average value of 11.182 Bq/L.

Table 4. Radionuclides concentrations in water samples from the study area [71].

S/no.	Location	Nature	Bed rock	40K (Bq/L)	238U (Bq/L)	232Th (Bq/L)
1	Ede	Hand dug	Pegmatite	9.03 ± 0.97	23.76 ± 0.31	10.10 ± 0.5
2	Ede	Hand dug	Pegmatite	15.71 ± 0.83	17.85 ± 0.22	7.30 ± 0.49
3	Ede	Hand dug	Pegmatite	23.82 ± 0.83	10.62 ± 0.22	19.84 ± 0.53
4	Ede	Hand dug	Pegmatite	10.08 ± 0.87	9.90 ± 0.23	14.62 ± 0.55
5	Ede	Hand dug	Pegmatite	27.74 ± 0.74	9.61 ± 0.302	8.38 ± 0.52
6	Ede	Hand dug	Pegmatite	21.58 ± 0.95	22.47 ± 0.30	20.97 ± 0.66
7	Ede	Hand dug	Pegmatite	16.61 ± 0.83	7.24 ± 0.24	11.14 ± 0.52
8	Ede	Hand dug	Pegmatite	17.18 ± 0.91	10.45 ± 0.25	8.54 ± 0.58
9	Ede	Hand dug	Pegmatite	13.63 ± 0.81	10.51 ± 0.25	4.08 ± 0.59
10	Ede	Hand dug	Pegmatite	16.11 ± 1.01	14.04 ± 0.23	6.58 ± 0.55
11	Iddo	Borehole	Grey gneiss	14.00 ± 0.96	13.46 ± 0.30	9.00 ± 0.55
12	Iddo	Borehole	Grey gneiss	4.53 ± 0.96	9.91 ± 0.29	6.58 ± 0.66
13	Ekuro	Hand dug	Quartzite	9.68 ± 0.77	15.21 ± 0.30	6.42 ± 0.53
14	Iwoye	Hand dug	Grey gneiss	21.21 ± 0.78	12.04 ± 0.23	12.25 ± 0.56
15	Ekuro	Hand dug	Quartzite	3.47 ± 1.01	11.77 ± 0.23	11.63 ± 0.67

This data demonstrates that Ede has a higher thorium-232 activity, surpassing the combined activity of the four other communities by around 0.632 Bq/L. The average activity values for Iddo and Ekuro are 7.79 ± 0.605 Bq/L and 9.025 ± 0.6 Bq/L, respectively. On the other hand, Iwoye demonstrates an activity value of 12.25 ± 0.56 Bq/L.

The analysis results demonstrated that the activity concentration for 40K varies from 3.47 ± 1.01 to 27.74 ± 0.74 Bq/L, with a normal of 14.96 Bq/L over the whole area. In Ede, the values range from 27.74 ± 0.74 to 9.03 ± 0.97 Bq/L, with an average of 17.149 Bq/L. The average concentration in Ede surpasses the regional average (average for all four communities). Samples from Iddo and Ekuro show average concentrations of 9.265 ± 0.96 Bq/L and 6.6 ± 0.89 Bq/L, respectively, while Iwoye has a concentration of 21.21 ± 0.78 Bq/L.

In general, there is increased activity observed in all of the samples, in spite of variations in the concentrations of the radionuclides across different locations. **Figure 10**. The concentration of potassium remains consistently high in about all of the samples, reaching its peak in sample 5 (Ede) and its lowest in sample 15 (Ekuro). The elevated activity of 40K can be attributed to the abundance of potassic or K-feldspar ($KAlSi_3O_8$), which is the second most predominant mineral in these felsic rocks. On the other hand, quartz (SiO_2), the most abundant mineral, does not host any other elements other than oxygen and silicon to a significant extent.

The uranium series exhibits its highest concentration in sample 1 (Ede) and its lowest concentration in sample 7 (Ede). Similarly, the thorium series reaches its peak concentration in sample 6 (Ede) and appears to have its least concentration in sample 9 (Ede). Notably, sample 6 in Ede demonstrates equal activity concentrations for all the radionuclides.

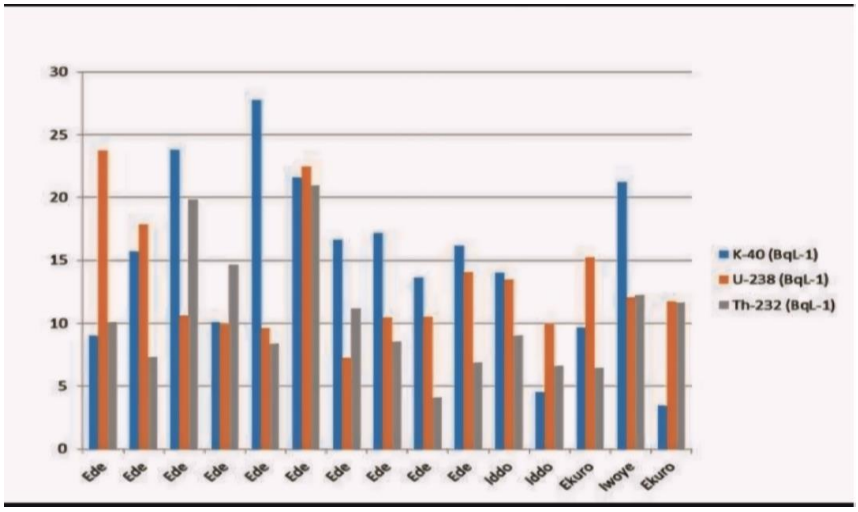

Figure 10. Bar chart showing radionuclides concentration in water samples from the study area [71].

3.3. Measurement of 226Ra in river water using liquid scintillation counting technique

A case study by Hamzah et al. [81].

Scintillation counting was used for measurement of 226Ra in water samples from Sungai Kelantan, mainly in the district of Kuala Krai.

3.3.1. Sampling site

Figure 11 shows a geological map of the Kelantan region, delineating the boundaries of the 10 area regions. The predominant geological features in Kelantan consist of undifferentiated acid intrusive rocks as well as formations from the Triassic and Permian periods. Furthermore, **Figure 12** outlines the particular areas where river water samples were collected within the Kuala Krai district.

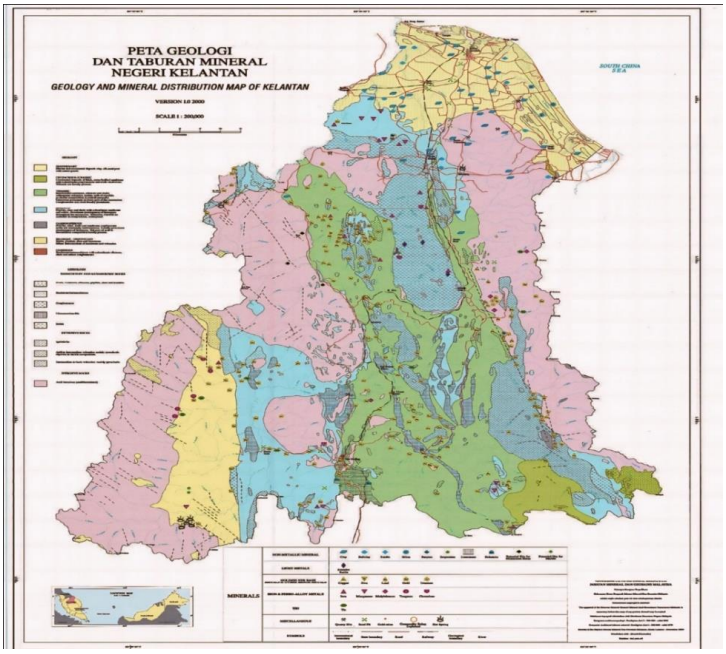

Figure 11. Geological map of Kelantan [81].

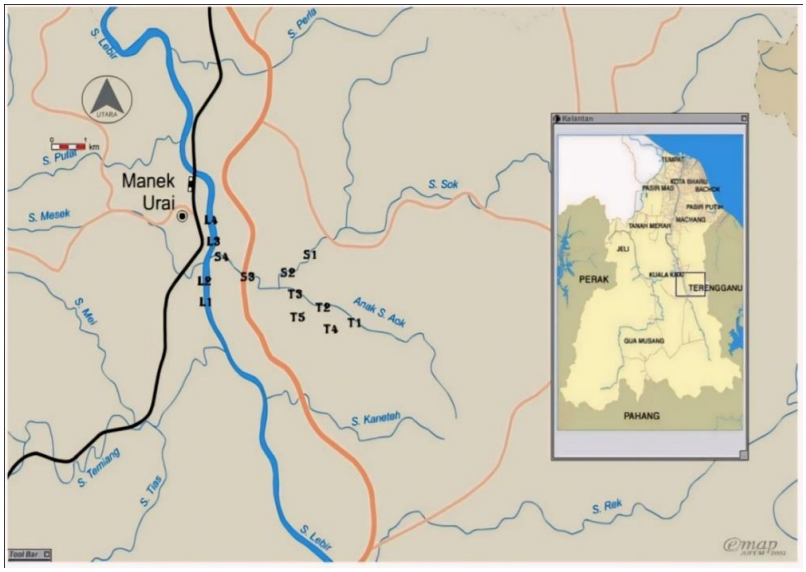

Figure 12. Area of sampling [81].

3.3.2. River water sample

To analyze the presence of 226Ra in a river sample, roughly 10 L of the untreated sample was carefully collected in a polyethylene bottle that had been completely cleaned with HNO_3 and distilled water. The collection of water samples was done at the midpoint of the river to guarantee their representativeness and to include the desired elements of interest, such as radionuclides. In order to protect the water and prevent any loss of radionuclides through sorption in the bottles, concentrated HNO_3 was promptly added to the raw sample at a ratio of 1 mL HNO_3 per 1 L of water [82].

These samples were obtained at a depth ranging from 0.01 to 0.3 m within the river. The water samples are passed through a membrane filter with a porosity of 0.47 μm and a diameter of 47 mm in order to remove suspended solids and impurities. In this way, 1 L of the filtered samples is transferred into Schott bottles, followed by the addition of 100 mL of scintillator to the samples.

3.3.3. Reagents and solutions

The scintillator was prepared by measuring 4.0 g of 2,5-diphenyloxazole (PPO) and 0.4 g of 1,4-bis(5-phenyloxazol-2-yl)-benzene (POPOP), which were then added to 1 liter of toluene of scintillation grade [83].

To guarantee a uniform dissolution in the solvent, the scintillator was stirred for a duration of 24 h. In this way, 100 mL of the scintillator was added to the 1 L water samples and allowed to incubate for a period of three weeks. Finally, 20.0 mL of the liquid scintillation cocktail was transferred into a polyethylene vial and promptly measured by liquid scintillation counting (LSC).

The liquid scintillation counter was utilized to measure the scintillation cocktail twice, with each cycle lasting 100 min. The counting method followed protocol 18 of Packard TRICAB 2700. The concentration of 226Ra was determined by calculating the total alpha peaks of 226Ra and its daughters (222Rn) in the alpha spectrum region [84].

3.3.4. Results

The range of these concentrations for the filtered sample is from 0.1095 Bq/L to

0.5483 Bq/L. Notably, the highest concentration is observed at the Manik Urai Bridge. It is worth saying that the activity concentrations of 226Ra from all 13 areas have surpassed the limit established by the Interim National Water Quality Standards for Malaysia (INWQS), which states that the activity concentration of 226Ra in water should not surpass 0.1 Bq/L. These findings suggest that 226Ra is dissolved in the water rather than merely being attached to suspended solids.

There are three particular sections of sampling in the study area, which are characterized by the small Sok River joining the Sok River and later joining the Lebir River. These rivers exhibit a progressive increase in size, starting from a small stream and gradually changing into a larger river. The collected information indicates a consistent pattern over all sections, where the activity concentration of 226Ra in each river section increases as the water flows downstream. This suggests that there may be a buildup of 226Ra in the water due to erosion within the river basin. **Figure 13a–c** depicts the measured activity concentrations of 226Ra in all sections of the study area.

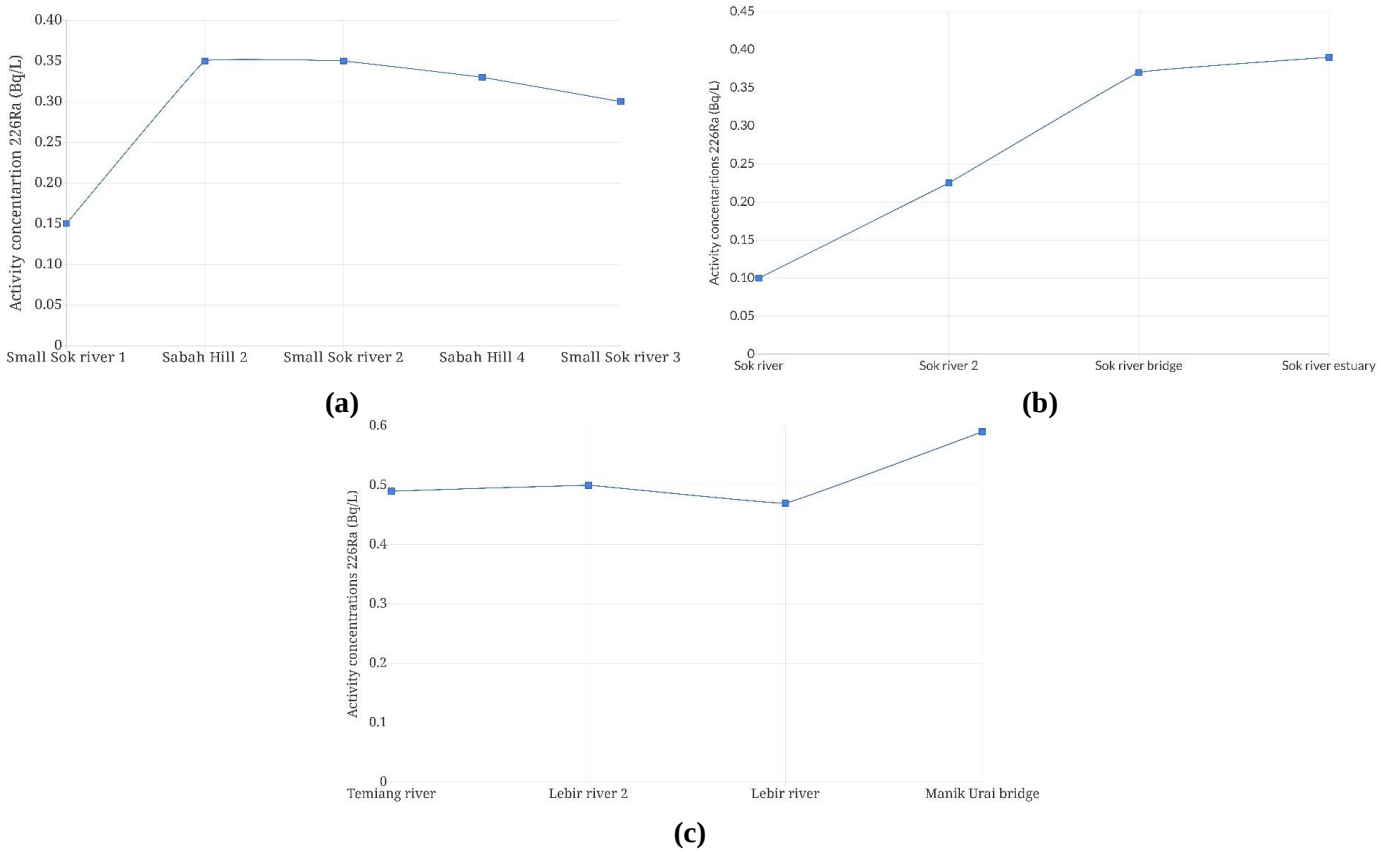

Figure 13. Activity concentrations of 226Ra measured along the 3 river sections in the study area [81].

Figure 14 illustrates the activity concentration of 226Ra over the three sections within the study area. The information reveals a recognizable pattern, with the highest activity concentration observed in the downstream sample. This suggests that various tributaries contribute varying amounts of 226Ra, influenced by the geological characteristics of the river basin. To find out the primary source of radium along this river, additional research is imperative.

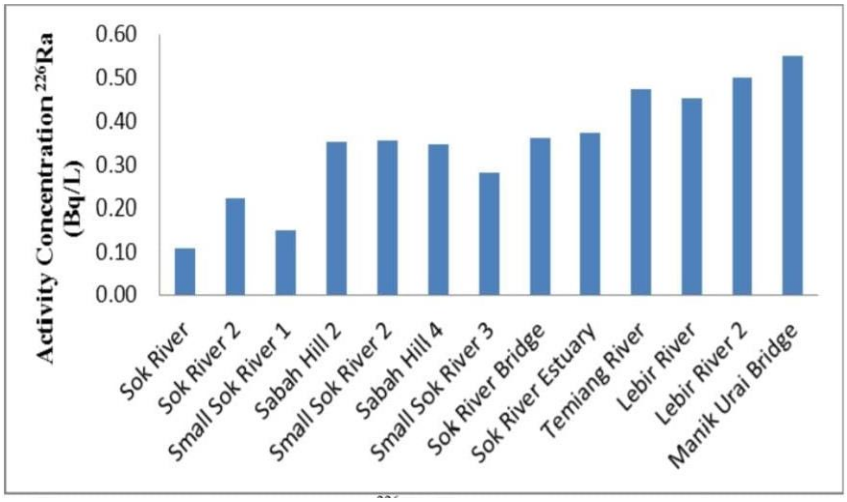

Figure 14. Activity concentration of 226Ra along 3 different sections in the study area [81].

In general, the samples show an activity concentration of 226Ra that surpasses the limit established in the INWQS. This can be attributed to the fact that the area, particularly the river basin, is situated within a granitic region that contains natural radionuclides. Among these radionuclides, 238U and 232Th play a significant role as they give rise to decay products that include 226Ra and 228Ra. However, due to its relatively short half-life, the contribution of 228Ra is considerably less significant compared to that of 226Ra. From a health risk perspective, the presence of radon and thoron, which are the decay products of radium, is of greater concern as they exist in gaseous form and can dissolve in water (**Table 5**).

Table 5. Activity concentration 222Rn and annual effective dose of 226Ra in river water from different locations in Kelantan [81].

Sample code	Ra (Bq/L)	Rn (Bq/L)	Estimated annual effective dose (mSv/year)
Lebir River			
L1	0.050 ± 0.7415	3.8911 ± 0.41	0.0964
L2	0.042 ± 0.4510	3.7540 ± 0.35	0.0922
L3	0.041 ± 0.4998	4.1577 ± 0.34	0.1022
L4	0.033 ± 0.5483	4.4326 ± 0.27	0.1121
Sok River			
S1	0.1095 ± 0.049	0.8836 ± 0.40	0.0224
S2	0.2203 ± 0.036	1.7834 ± 0.29	0.0450
S3	0.3613 ± 0.039	2.9056 ± 0.32	0.0739
S4	0.3732 ± 0.030	3.0353 ± 0.24	0.0763
Small Sok River			
T1	0.1491 ± 0.045	1.2073 ± 0.37	0.0305
T2	0.3569 ± 0.031	2.8880 ± 0.25	0.0730
T3	0.2803 ± 0.034	2.2652 ± 0.28	0.0573
T4	0.3524 ± 0.033	2.8400 ± 0.27	0.0720
T5	0.3466 ± 0.033	2.8211 ± 0.27	0.0708

When assessing the annual effective dose in the river water samples, it is expected that there will be a few contributions from naturally occurring radionuclides in the granitic area, as well as through the decay series of uranium and thorium in the soil [85].

The annual effective dose falls within the range of 0.0224–0.1531 mSv/year, as shown in **Table 1**, which is determined through the following equation: Yearly effective dose = 730 L/yr × 2.8×10^{-4} mSv/Bq × activity concentration of 226Ra (Bq/L).

The calculation of the annual effective dosage for water consumption by adults in this region, who depend on river water as their primary water supply, was conducted. It was determined that the annual drinking amount is 730 L/yr, assuming that an adult consumes 2 L of water per day. The dose conversion factor for 226Ra is 2.8×10^{-7} Sv/Bq [86]. As per the regulation set forth by the Polish Ministry of Health in 2002, the annually permissible effective dosage for all radionuclides, with the exception of tritium, must not surpass 0.010 mSv/year [86].

4. Health implications

The terrestrial environment is full of naturally occurring radioactive material, or NORM, which can be hazardous to human health [87]. Globally, the typical person receives 3.0 mSv annually. Radiation exposure from radon and thoron sources is the biggest source of dosage among all public radiation exposure sources. 42% of the annual absorbed dose globally is attributed to exposure to these radionuclides in the air and water. Upon entering the body, radionuclides are dispersed differently according to their shapes, chemical characteristics, and exposure pathways. When assessing the possible impacts of exposure, this causes variable accumulation and excretion that needs to be taken into consideration. It is significant to remember that, on average, NORM accounts for only about half of the radiation exposure that the general public experiences; the other half is attributed to man-made sources, mostly medical treatments [88].

The most concentrated dose of NORM is obtained from inhaling radon and thoron into the lungs. The decay of these radionuclides exposes the mouth, airways, and lung tissue to alpha particles directly after inhalation. Because of their incredibly short half-lives (microseconds to minutes), the decay products of radon and thoron can expose lung tissue to additional radiation in addition to the initial decay of these radionuclides in the lungs. They can even dissolve into the airway surface fluid and be absorbed into the blood stream through the lung [89]. The primary means of ingesting radionuclides is through contaminated drinking water and radionuclide-containing food. Once within the gastrointestinal tract, radionuclides can be taken up by active transport, passive diffusion, or both [90].

The largest single health effect of NORM exposure is the development and encouragement of cancer. The strongest evidence for the link between environmental exposure to NORM and cancer comes from exposure to 220Rn and 222Rn. Numerous epidemiological studies conducted on U miners and the general public indicate that there is probably a causal relationship between lung cancer and exposure to 220Rn/222Rn [91,92].

5. Conclusion

Understanding radioactivity begins with understanding its origin, whether it is primordial or cosmogenic. Radioactivity surrounds humans from each direction, and in this review, we tried to concentrate on its geological direction and how it can affect the environment and humans. Exposure to radiation can lead to many health risks by exceeding the permissible limit of radiation in the air, water, and dust. Spectrometry scientists have developed applications in which we can measure the emitted radiation emanating from rocks.

We shed light on some of the methodologies that are used to measure NORM radiation and how they work, their advantages and disadvantages, and their theories, semiconductor detectors like the high-Purity germanium detector and the thallium activated sodium iodide detector NaI(Tl), the liquid scintillation counting (LSC) technique.

Using the environmental samples matrix standard with both single-photon emitting nuclides mixed standard QCY40 containing 210Pb, 241Am, 109Cd, and 57Co, and the second QCY48 containing 241Am, 109Cd, Co57, 139Ce, 113Sn, 85Sr, 137Cs, 88Y, and 60Co, the absolute full-energy peak efficiency of high purity germanium (HPGe) detectors has been measured between (46, 54 and 1836) keV. The energy of the gamma rays, the geometry, the density, the height of the soil sample, and the detector characterization all affect efficiency.

In the first case study, the results of measuring radioactivity with a NaI(Tl) detector were compared to laboratory measurements made on geological samples using HPGe detectors. This is an important issue for analytical laboratories as it is the result of the IAEA procedure's proficiency test for all analytical determinations that are received as "acceptable" for all radionuclides. It should be mentioned that there are noticeable variations in both detector parameters' results. One possible cause of the mean mismatch between the NaI(Tl) and HPGe detectors could be an unidentified sample material.

Using a gamma ray spectrometer setup, the complete energy peak efficiencies of the NaI(Tl) detector were experimentally determined in the energy range of 1460 keV to 2614 keV. The results show that despite its poor energy resolution, a NaI(Tl) detector has a high efficiency, making it suitable for use in a variety of research applications.

In the second case study, the unusually high levels of radionuclides found in ground water in Ede and the surrounding settlements can only be attributed to geology, not to any other human activity. Therefore, it is necessary to conduct a regional radionuclide evaluation of groundwater in order to ascertain the spatial extent of these anomalous concentrations, the effects they have on local organic species, and any potential groundwater treatment plans before they are used. We also propose that comparable studies be conducted in pegmatite bedrock regions worldwide, since high activity might not be completely ruled out given that these rocks had a similar fractional crystallization sequence and focused on high concentrations of big ion lithophile elements.

In radionuclide metrology, liquid scintillation counting techniques are frequently applied for both the standardization of pure beta and an increasing number of

radionuclides with more complex decay schemes. The primary benefit of LSC is its ability to quickly and simply prepare sources, which enables short-lived radionuclides to be standardized. The invention of the free parameter model allows one to use a tracer methodology, like the CIEMAT/NIST method, to determine detection efficiency. The majority of national radionuclide metrology laboratories currently employ LSC procedures, which have resulted in a growing number of radionuclides being standardized over time. While there is still need for improvement in quantitative LSC procedures, LSC standardization techniques have advanced significantly and are now widely used in radionuclide metrology.

In the third case study, the samples of river water show that the concentration of 226Ra in the samples is higher than the INTERIM National Water Quality Standards for Malaysia (0.1 Bq/L). The values for the annual effective dose of water have also surpassed the 0.01 mSv/yr international guideline value.

There are naturally occurring radioactive materials everywhere in the environment, and both the general population and radiation workers are at risk for health problems. With 220Rn and 222Rn gas accounting for 42% of the global public radiation dose, exposure to these gases in the air presents the greatest risk to public health among NORM. changes done to the environment, like resource extraction and drilling. Reducing the overall risk of cancer and limiting possible exposure require regulating the spread of NORM through human activities.

Conflict of interest: The authors declare no conflict of interest.

References

1. Martin JE. Naturally Occurring Radiation and Radioactivity. In: Physics for Radiation Protection. Wiley-VCH Verlag GmbH & Co. KGaA; 2013.
2. Isaksson M. Methods of measuring radioactivity in the environment (No. LUNFD6-NFFR--1017). Lund Univ. (Sweden). Dept. of Nuclear Physics; 1997.
3. Abedin MdJ, Khan R. NORMs distribution in the dust samples from the educational institutions of Megacity Dhaka, Bangladesh: Radiological risk assessment. Journal of Hazardous Materials Advances. 2022; 8: 100155. doi: 10.1016/j.hazadv.2022.100155
4. Abedin MdJ, Khan R. Primordial radionuclides in the dust samples from the educational institutions of central Bangladesh: radiological risk assessment. Heliyon. 2022; 8(11): e11446. doi: 10.1016/j.heliyon.2022.e11446
5. Khandaker MU, Mohd Nasir NL, Asaduzzaman K, et al. Evaluation of radionuclides transfer from soil-to-edible flora and estimation of radiological dose to the Malaysian populace. Chemosphere. 2016; 154: 528-536. doi: 10.1016/j.chemosphere.2016.03.121
6. Khandaker MU, Asaduzzaman K, Sulaiman AFB, et al. Elevated concentrations of naturally occurring radionuclides in heavy mineral-rich beach sands of Langkawi Island, Malaysia. Marine Pollution Bulletin. 2018; 127: 654-663. doi: 10.1016/j.marpolbul.2017.12.055
7. Khan R, Islam HMT, Apon MAS, et al. Environmental geochemistry of higher radioactivity in a transboundary Himalayan River sediment (Brahmaputra, Bangladesh): potential radiation exposure and health risks. Environmental Science and Pollution Research. 2022; 29(38): 57357-57375. doi: 10.1007/s11356-022-19735-5
8. Khan R, Haydar MA, Saha S, et al. (2022). Spatial distribution and radiological risk quantification of natural radioisotopes in the St. Martin's Island, Bangladesh. In: Soil Health and Environmental Sustainability: Application of geospatial technology. Cham: Springer International Publishing; pp. 369-388.
9. Habib MA, Basuki T, Miyashita S, et al. Distribution of naturally occurring radionuclides in soil around a coal-based power plant and their potential radiological risk assessment. Radiochimica Acta. 2018; 107(3): 243-259. doi: 10.1515/ract-2018-3044

10. Ionizing radiation and health effects. Available online: https://www.who.int/news-room/fact-sheets/detail/ionizing-radiation-and-health-effects (accessed on 3 April 2024).
11. Arogunjo AM, Höllriegl V, Giussani A, et al. Uranium and thorium in soils, mineral sands, water and food samples in a tin mining area in Nigeria with elevated activity. Journal of Environmental Radioactivity. 2009; 100(3): 232-240. doi: 10.1016/j.jenvrad.2008.12.004
12. Abbasi MN, Tufail M, Chaudhry MM. Assessment of heavy elements in suspended dust along the Murree Highway near capital city of Pakistan. World Applied Science Journal. 2013; 21(9): 1266-1275.
13. Kohman TP, Saito N. Radioactivity in Geology and Cosmology. Annual Review of Nuclear Science. 1954; 4(1): 401-462. doi: 10.1146/annurev.ns.04.120154.002153
14. Bastos RO, Appoloni CR, Pinese JPP, et al. Gamma Radiation Dose Rate in Air due to Terrestrial Radionuclides in Southern Brazil: Synthesis by Geological Units and Lithotypes Covered by the Serra do Mar Sul Aero-Geophysical Project. AIP Conference Proceedings. 2018; 1034(1): 403-406.
15. Bastos RO, Pascholati EM. Environmental gamma radiation in municipalities of Eastern of São Paulo State, Brazil. Terrae. 2005; 2(1-2): 37-45.
16. Dickson BL, Scott KM. Interpretation of aerial gamma-ray surveys-adding the geochemical factors. AGSO Journal of Australian Geology and Geophysics. 1997; 17.
17. Durrance EM. Radioactivity in geology: principles and applications. United States: N.; 1986.
18. Tarim UA, Gürler O. Source-to-detector distance dependence of efficiency and energy resolution of a 3"x3" NaI (Tl) detector. Avrupa Bilim ve Teknoloji Dergisi. 2018; (13): 103-107. doi: 10.31590/ejosat.443565
19. Sharma RK. Various spectroscopic techniques. Environmental Pollution: Monitoring Modelling and Control. Studium Press; 2017. pp. 181-206.
20. Vargas MJ, Timón AF, Díaz NC, Sánchez DP. Influence of the geometrical characteristics of an HpGe detector on its efficiency. Journal of Radioanalytical and Nuclear Chemistry. 2002; 253.
21. Alnour IA, Wagiran H, Ibrahim N, et al. New approach for calibration the efficiency of HpGe detectors. AIP conference proceedings. 2014; 1584(1): 38-44.
22. Knoll GF. Radiation detection and measurement. John Wiley & Sons; 2010.
23. Ngaram S, Baffa A, And I, Yunusa M. Determination of natural radionuclide using HPGe detectors. Journal of Environment, Technology & Sustainable Agriculture. 2017; 1: 14-22.
24. Guo Y, Wang Q, Kawazoe Y, et al. A New Silicon Phase with Direct Band Gap and Novel Optoelectronic Properties. Scientific Reports. 2015; 5(1). doi: 10.1038/srep14342
25. Leadbeater T. Lecture Notes on Particle Detectors. Birmingham: Physics and Astronomy. University of Birmingham; 2015.
26. Arif K, Malik AH. Monte Carlo EGS5 simulationsof High Purity Germanium (HPGe) detector. In: Proceedings of the 2015 Power Generation System and Renewable Energy Technologies (PGSRET). pp. 1-3.
27. High Purity Germanium Detectors—HPGe. Available online: https://www.nuclear-power.com/nuclear-engineering/radiation-detection/semiconductor-detectors/high-purity-germanium-detectors-hpge/ (accessed on 3 April 2024).
28. Saegusa J, Kawasaki K, Mihara A, et al. Determination of detection efficiency curves of HPGe detectors on radioactivity measurement of volume samples. Applied Radiation and Isotopes. 2004; 61(6): 1383-1390. doi: 10.1016/j.apradiso.2004.04.004
29. Vargas MJ, Timón AF, Dıaz NC, Sánchez DP. Monte Carlo simulation of the self-absorption corrections for natural samples in gamma-ray spectrometry. Applied Radiation and Isotopes. 2002; 57(6): 893-898.
30. Vargas MJ, Díaz NC, Sánchez DP. Efficiency transfer in the calibration of a coaxial p-type HpGe detector using the Monte Carlo method. Applied Radiation and Isotopes. 2003; 58(6): 707-712.
31. Vidmar T, Korun M, Likar A, Martinčič R. A semi-empirical model of the efficiency curve for extended sources in gamma-ray spectrometry. Nuclear Instruments and Methods in Physics Research Section A: Accelerators, Spectrometers, Detectors and Associated Equipment. 2001; 470(3): 533-547.
32. Al-Masri MS, Aba A, Al-Hamwi A, et al. Preparation of in-house reference soil sample containing high levels of naturally occurring radioactive materials from the oil industry. Applied Radiation and Isotopes. 2004; 61(6): 1397-1402. doi: 10.1016/j.apradiso.2004.04.007
33. Melquiades FL, Appoloni CR. Self-absorption correction for gamma spectrometry of powdered milk samples using Marinelli beaker. Applied Radiation and Isotopes. 2001; 55(5): 697-700.

34. San Miguel EG, Pérez-Moreno JP, Bolívar JP, et al. 210Pb determination by gamma spectrometry in voluminal samples (cylindrical geometry). Nuclear Instruments and Methods in Physics Research Section A: Accelerators, Spectrometers, Detectors and Associated Equipment. 2002; 493(1-2): 111-120.
35. Abbas MI, Selim YS. Calculation of relative full-energy peak efficiencies of well-type detectors. Nuclear Instruments and Methods in Physics Research Section A: Accelerators, Spectrometers, Detectors and Associated Equipment. 2002; 480(2-3): 651-657.
36. Harb S, Salahel Din K, Abbady A. Study of efficiency calibrations of HPGe detectors for radioactivity measurements of environmental samples. In: Proceedings of the 3rd Environmental Physics Conference; 19-23 February 2008; Aswan, Egypt.
37. Akkurt I, Gunoglu K, Arda SS. Detection Efficiency of NaI(Tl) Detector in 511–1332 keV Energy Range. Science and Technology of Nuclear Installations. 2014; 2014: 1-5. doi: 10.1155/2014/186798
38. El-Gamal H, Negm H, Hasabelnaby M. Detection efficiency of NaI (Tl) detector based on the fabricated calibration of HPGe detector. Journal of Radiation Research and Applied Sciences. 2019; 12(1): 360-366. doi: 10.1080/16878507.2019.1672313
39. Rathore V, Senis L, Andersson Sundén E, et al. Geometrical optimisation of a segmented HPGe detector for spectroscopic gamma emission tomography—A simulation study. Nuclear Instruments and Methods in Physics Research Section A: Accelerators, Spectrometers, Detectors and Associated Equipment. 2021; 998: 165164. doi: 10.1016/j.nima.2021.165164
40. Ahmadi S, Ashrafi S, Yazdansetad F, et al. A computational modelling of low-energy gamma ray detection efficiency of a cylindrical NaI(Tl) detector. Radiation Physics and Chemistry. 2021; 188: 109581. doi: 10.1016/j.radphyschem.2021.109581
41. Tsoulfanidis N. Nuclear Fission Reactors. Nuclear Technology. 1983; 63(1): 187-187. doi: 10.13182/nt83-a33318
42. Böhlen TT, Cerutti F, Chin MPW, et al. The FLUKA Code: Developments and Challenges for High Energy and Medical Applications. Nuclear Data Sheets. 2014; 120: 211-214. doi: 10.1016/j.nds.2014.07.049
43. Ferrari A, Sala PR, Fasso A, Ranft J. FLUKA: A Multi-particle Transport Code. Stanford Linear Accelerator Center, Stanford University; 2005.
44. Tekin HO. MCNP-X Monte Carlo Code Application for Mass Attenuation Coefficients of Concrete at Different Energies by Modeling 3 × 3 Inch NaI(Tl) Detector and Comparison with XCOM and Monte Carlo Data. Science and Technology of Nuclear Installations. 2016; 2016: 1-7. doi: 10.1155/2016/6547318
45. Akkurt İ, Tekin HO, Mesbahi A. Calculation of Detection Efficiency for the Gamma Detector using MCNPX. Acta Physica Polonica A. 2015; 128(2B): B-332-B-335. doi: 10.12693/aphyspola.128.b-332
46. Salgado CM, Brandão LEB, Schirru R, et al. Validation of a NaI(Tl) detector's model developed with MCNP-X code. Progress in Nuclear Energy. 2012; 59: 19-25. doi: 10.1016/j.pnucene.2012.03.006
47. Mouhti I, Elanique A, Messous MY, et al. Validation of a NaI(Tl) and LaBr3(Ce) detector's models via measurements and Monte Carlo simulations. Journal of Radiation Research and Applied Sciences. 2018; 11(4): 335-339. doi: 10.1016/j.jrras.2018.06.003
48. Akkurt İ, Waheed F, Akyildirim H, et al. Performance of NaI(Tl) detector for gamma-ray spectroscopy. Indian Journal of Physics. 2021; 96(10): 2941-2947. doi: 10.1007/s12648-021-02210-1
49. Tekin HO, ALMisned G, Issa SAM, et al. Calculation of NaI(Tl) detector efficiency using 226Ra, 232Th, and 40K radioisotopes: Three-phase Monte Carlo simulation study. Open Chemistry. 2022; 20(1): 541-549. doi: 10.1515/chem-2022-0169
50. Hendriks PHGM, Limburg J, De Meijer RJ. Full-spectrum analysis of natural γ-ray spectra. Journal of Environmental Radioactivity. 2001; 53(3): 365-380.
51. Løvborg L, Christiansen EM, Bøtter-Jensen L, Kirkegaard, P. Pad facility for the calibration of gamma-ray measurements on rocks (No. RISO-R—454). Risoe National Lab.; 1981.
52. Agency IE. The radiological accident in San Salvador: A Report. International Atomic Energy Agency; 1990.
53. Biere PE, Aina JO, Olaoye MO, et al. Calibration of a 5 × 5 NaI(Tl) for Prompt In-Situ Gamma-ray Spectrometry System. Materials and Geoenvironment. 2021; 68(1): 1-5. doi: 10.2478/rmzmag-2021-0001
54. Boson J. Improving accuracy of in situ gamma-ray spectrometry [PhD thesis]. Radiation Physics Umeå University; 2008.
55. Beck HL, Gogolak C, DeCampo J. In situ Ge (Li) and NaI (T1) gamma-ray spectrometry (No. HASL-258). United States Atomic Energy Commision, New York, NY (United States). Health and Safety Lab.; 1972.
56. Kallmann H. Scintillation Counting with Solutions. Physical Review. 1950; 78(5): 621-622. doi: 10.1103/physrev.78.621.2
57. Reynolds GT, Harrison FB, Salvini G. Liquid Scintillation Counters. Physical Review. 1950; 78(4): 488-488. doi: 10.1103/physrev.78.488

58. Pochwalski K, Radoszewski T. Disintegration rate determination by liquid scintillation counting using the triple to double coincidence ratio (TDCR) method. Institute of Nuclear Research, Warsaw, INR; 1848.
59. Malonda AG, Garcia-Toraño E. Evaluation of counting efficiency in liquid scintillation counting of pure β-ray emitters. The International Journal of Applied Radiation and Isotopes. 1982; 33(4): 249-253.
60. Introduction Liquid Scintillation—mn/safe/nukwik. Available online: https://wiki.uio.no/mn/safe/nukwik/index.php/Introduction_Liquid_Scintillation (accessed on 3 April 2024).
61. Broda R, Cassette P, Kossert K. Radionuclide metrology using liquid scintillation counting. Metrologia. 2007; 44(4): S36-S52. doi: 10.1088/0026-1394/44/4/s06
62. Peng CT, Li U. Analysis of solvent components in commercial liquid scintillation cocktails. LSC. 1992; 92: 157.
63. Hung NQ, Chuong HD, Vuong LQ, et al. Intercomparison NaI(Tl) and HPGe spectrometry to studies of natural radioactivity on geological samples. Journal of Environmental Radioactivity. 2016; 164: 197-201. doi: 10.1016/j.jenvrad.2016.07.035
64. Osprey® Universal Digital MCA Tube Base for Scintillation Spectrometry. Available online: https://www.mirion.com/products/technologies/spectroscopy-scientific-analysis/gamma-spectroscopy/detector-electronics/osprey-universal-digital-mca-tube-base-for-scintillation-spectrometry (accessed on 3 April 2024).
65. Lépy MC. Presentation of the COLEGRAM software. Note Technique LHNB/04/26. 2004. Available online: http://www.lnhb.fr/pdf/NT_04-26_Colegram.pdf (accessed on 12 January 2024).
66. IAEA. certification of IAEA gamma spectrometry reference materials, RGU-1, RGTh-1 and RGK-1, Report-IAEA/RL/148. International Atomic Energy Agency; 1987.
67. Gilmore G. Practical gamma-ray spectroscopy. John Wiley & Sons; 2008.
68. Lépy MC, Ferreux L, Hamon C, Plagnard J. ACORES yield curve adjustment software. Technical note LNHB. Available online: http://www.lnhb.fr/en/
69. GUM: Guide to the Expression of Uncertainty in Measurement—Evaluation of measurement data. Available online: https://www.bipm.org/documents/20126/2071204/JCGM_100_2008_E.pdf/cb0ef43f-baa5-11cf-3f85-4dcd86f77bd6 (accessed on 12 January 2024).
70. Shakhashiro A, Mabit L. Results of an IAEA inter-comparison exercise to assess 137Cs and total 210Pb analytical performance in soil. Applied Radiation and Isotopes. 2009; 67(1): 139-146. doi: 10.1016/j.apradiso.2008.07.014
71. Adetunji A, Olorunfemi AO, Abe O, et al. Anomalous concentrations of radionuclides in the groundwater of Ede area, southwestern Nigeria: a direct impact of geology. Environmental Earth Sciences. 2018; 77(17). doi: 10.1007/s12665-018-7799-2
72. Lydie RM, Nemba RM. Quantitative determination of 226Ra and 228Ra in reservoir and tap water in Yaoundé area, Cameroon. Glob. J. envir. Res. 2008; 2(3): 110-113.
73. Jibiri NN, Mbawanku AO, Oridata AA, Ujiagbedion C. Natural radionuclide concentration levels in soil and water around cement factory. Ewekoro, Ogun state. Nigeria Journal of physics. 1999; 11: 12-16.
74. Ajayi IR, Ajayi OS, Fusuyi AS. The natural radioactivity of surface soils in Ijero-Ekiti, Nigeria. Nig. J. Phys. 1995; 7: 101-103.
75. Farai IP, Sanni AO. Year-long variability of Rn-222 in a groundwater system in Nigeria. Journal of African Earth Sciences (and the Middle East). 1992; 15(3-4): 399-403.
76. Ahmed NK. Natural Radioactivity of Ground and Drinking Water in Some Areas of Upper Egypt. Turkish Journal of Engineering & Environmental Sciences. 2004; 28(6).
77. Nasirian M, Bahari I, Abdullah P. Assessment of natural radioactivity in water and sediment from Amang (tin tailing) processing ponds. Malays J Anal Sci. 2008; 12(1): 150-159.
78. Lydie RM, Nemba RM. The annual effective dose due to natural radionuclides in the reservoir and tap water in Yaoundé area, Cameroon. The South Pacific Journal of Natural and Applied Sciences. 2009; 27(1): 61. doi: 10.1071/sp09011
79. Ajayi OS, Adesida G. Radioactivity in some sachet drinking water samples produced in Nigeria. Iran. J. Radiat. Res. 2009; 7(3): 151-158.
80. Nwankwo LI. Study of natural radioactivity of groundwater in Sango-Ilorin, Nigeria. Journal of Physical Science and Application 2012; 2(8): 289.
81. Rahman SAA. Measurement of 226Ra in river water using liquid scintillation counting technique. Journal of Nuclear and Related Technologies. 2010; 7(02): 12-23.
82. de Oliveira J, Mazzilli BP, de Oliveira Sampa MH, Bambalas E. Natural radionuclides in drinking water supplies of Sao

Paulo State, Brazil and consequent population doses. Journal of Environmental Radioactivity. 2001; 53(1): 99-109.
83. Borai EH, Lasheen YF, El-Sofany EA, et al. Separation and subsequent determination of low radioactivity levels of radium by extraction scintillation. Journal of Hazardous Materials. 2008; 156(1-3): 123-128. doi: 10.1016/j.jhazmat.2007.12.004
84. Kim YJ, Kim CK, Lee JI. Simultaneous determination of 226Ra and 210Pb in groundwater and soil samples by using the liquid scintillation counter-suspension gel method. Applied Radiation and Isotopes. 2001; 54(2): 275-281.
85. Lasheen YF, Seliman AF, Abdel-Rassoul AA. Simultaneous measurement of 226Ra and 228Ra in natural water by liquid scintillation counting. Journal of Environmental Radioactivity. 2007; 95(2-3): 86-97. doi: 10.1016/j.jenvrad.2007.02.002
86. Kozłowska B, Walencik A, Dorda J, et al. Uranium, radium and 40K isotopes in bottled mineral waters from Outer Carpathians, Poland. Radiation Measurements. 2007; 42(8): 1380-1386. doi: 10.1016/j.radmeas.2007.03.004
87. May D, Schultz MK. Sources and Health Impacts of Chronic Exposure to Naturally Occurring Radioactive Material of Geologic Origins. Practical Applications of Medical Geology. 2021; 403-428.
88. NCRP. Ionizing radiation exposure of the population of the United States. NCRP; 2006.
89. Marsh JW, Bailey MR. A review of lung-to-blood absorption rates for radon progeny. Radiation Protection Dosimetry. 2013; 157(4): 499-514. doi: 10.1093/rpd/nct179
90. Taylor D, Bligh P, Duggan M. The absorption of calcium, strontium, barium and radium from the gastrointestinal tract of the rat. Biochemical Journal. 1962; 83(1): 25-29. doi: 10.1042/bj0830025
91. Lubin JH, Boice JD, Edling C, et al. Lung Cancer in Radon-Exposed Miners and Estimation of Risk from Indoor Exposure. JNCI Journal of the National Cancer Institute. 1995; 87(11): 817-827. doi: 10.1093/jnci/87.11.817
92. Field RW, Steck DJ, Smith BJ, et al. Residential Radon Gas Exposure and Lung Cancer: The Iowa Radon Lung Cancer Study. American Journal of Epidemiology. 2000; 151(11): 1091-1102. doi: 10.1093/oxfordjournals.aje.a010153